Spatially displaced excitation contributes to the encoding of interrupted motion by the retinal direction-selective circuit

Jennifer Ding[1,2], Albert Chen[3], Janet Chung[2], Hector Acaron Ledesma[4], Mofei Wu[2], David M. Berson[5], Stephanie E. Palmer[1,3,6]*, Wei Wei[1,2,6]*

1. Committee on Neurobiology Graduate Program, The University of Chicago
2. Department of Neurobiology, The University of Chicago
3. Department of Organismal Biology, The University of Chicago
4. Graduate Program in Biophysical Sciences, The University of Chicago
5. Department of Neuroscience and Carney Institute for Brain Science, Brown University
6. Grossman Institute for Neuroscience, Quantitative Biology and Human Behavior, The University of Chicago

*Co-corresponding authors: weiw@uchicago.edu; sepalmer@uchicago.edu

Abstract

Spatially distributed excitation and inhibition collectively shape a visual neuron's receptive field (RF) properties. In the direction-selective circuit of the mammalian retina, the role of strong null-direction inhibition of On-Off direction-selective ganglion cells (ON-OFF DSGCs) on their direction selectivity is well-studied. However, how excitatory inputs influence the On-Off DSGC's visual response is underexplored. Here, we report that On-Off DSGCs have a spatially displaced glutamatergic receptive field along their preferred-null motion axis. This displaced receptive field contributes to DSGC null-direction spiking during interrupted motion trajectories. Theoretical analyses indicate that population responses during interrupted motion may help populations of On-Off DSGCs signal the spatial location of moving objects in complex, naturalistic visual environments. Our study highlights that the direction-selective circuit exploits separate sets of mechanisms under different stimulus conditions, and these mechanisms may help encode multiple visual features.

Introduction

How do sensory systems convert sensory inputs into behaviorally relevant neural signals? This question has been extensively investigated in the early visual system, where a neuron's responses to a set of parameterizable visual stimuli can be systematically probed to reveal a cell's receptive field (RF) properties in space and time. It has been increasingly appreciated that different visual stimuli can engage different mechanisms to shape the neuronal RF even at the earliest stage of visual processing in the retina. The transformation from the visual input to a retinal ganglion cell's spiking output is influenced by spatiotemporal patterns of stimuli in both the RF center and surround regions, highlighting the necessity of using diverse, ethologically relevant visual stimuli for delineating RF properties and for ultimately understanding neural coding of the animal's natural environment (Chiao and Masland, 2003; Demb et al., 1999; Deny et al., 2017; Huang et al., 2019; Ölveczky et al., 2003; Takeshita and Gollisch, 2014; Turner et al., 2018).

Direction-selective ganglion cells (DSGCs) in the mammalian retina are well-studied for their motion direction selectivity. A DSGC fires maximally to visual stimuli moving across its RF in its preferred direction and is inhibited from firing by stimuli moving in the opposite, null direction (Barlow and Hill, 1963; Barlow and Levick, 1965). The direction-selective spiking is largely attributed to the GABAergic input from the starburst amacrine cell (SAC). SAC dendrites are inherently direction-selective, as they are activated by centrifugal motion, or motion from soma to dendritic tip (Euler et al., 2002). Additionally, only SAC dendrites that extend along the null direction of the DSGC selectively make GABAergic synapses with the DSGC (Briggman et al., 2011; Fried et al., 2002; Lee and Zhou, 2010; Wei et al., 2011; Yonehara et al., 2011). Both the intrinsic properties of the SAC and the 'antiparallel' wiring patterns between the SAC and the DSGC are necessary for a strong null-direction inhibition onto the DSGC. The asymmetry of inhibition evoked by motion in the preferred and null directions is important for the DSGC's direction selectivity (Pei et al., 2015; Taylor and Vaney, 2002). The most well-studied DSGC type, the On-Off DSGC, prefers motion in one of the four cardinal directions (Oyster and Barlow, 1967; Sabbah et al., 2017). They have bistratified dendritic arbors in the On and Off sublamina of the inner plexiform layer (IPL) to extract motion directions of bright and dark signals, respectively (**Figure 1A**) (Famiglietti 1983; He and Masland, 1998; Kittila and Massey, 1997).

The RF of On-Off DSGCs has been studied with conventional visual stimuli such as stationary and moving spots, bars, and gratings. For motion stimuli that traverse across the entire RF, On-Off DSGC responses remain direction-selective over a broad range of contrast, luminance, speed, and background noise levels (Barlow and Levick, 1965; Chen et al., 2016; Grzywacz and Amthor, 2007; Lipin et al., 2015;

Sethuramanujam et al., 2016; Sivyer et al., 2010). However, motion stimuli restricted to the distal RF subregion on the preferred side (defined as the side from which the preferred-direction moving stimulus approaches the RF) can elicit non-directional firing (He et al., 1999; He and Masland, 1998; Rivlin-Etzion et al., 2011; Trenholm et al., 2011). Based on the responses to moving stimuli presented to different subregions of the DSGC RF, the cell's RF structure can be viewed as consisting of multiple 'DS subunits' and a 'non-DS zone' at the edge of the preferred side. However, the neural mechanisms underlying the modular and heterogenous RF subunits of On-Off DSGCs have not been elucidated. Furthermore, the functional significance of this fine RF structure is not clear.

In this study, we investigated the spatial RF structure of the mouse On-Off DSGC subtype that prefers motion in the posterior direction of the visual field (pDSGC). We found that the pDSGC spiking RF is skewed towards the preferred side of the cell for both stationary and moving stimuli, even in the absence of SAC-mediated inhibition. Combining anatomical and functional analyses, we found a spatially non-uniform glutamatergic excitatory conductance that contributes to this spatial displacement. As a result of the displaced RF, moving stimuli that only activate the preferred side of the pDSGC RF trigger robust firing during both preferred and null direction motion. Theoretical analyses of the On-Off DSGC population response allow us to speculate about the ethological relevance of the displaced RF in processing complex natural scenes, suggesting that it can allow for better estimation of object location when a moving object emerges from behind an occluder. We term this type of motion 'interrupted motion' to distinguish it from more standard smooth motion stimuli. This phenomenon might also allow synchronous firing from different subtypes of DSGCs to serve as a useful alarm signal in complex scenes.

Results

Glutamatergic excitation of the On-Off pDSGC is spatially asymmetric relative to the soma

To investigate the spatial distribution of excitatory inputs to On-Off pDSGCs, we targeted pDSGCs in the Drd4-GFP transgenic mouse line. Bright stationary spots were presented to the periphery of the DSCF RF and the spiking responses were recorded. These spots were 110 μm in diameter and centered 165 μm from the soma of the recorded DSGC (**Figure 1B**, schematic). Measurement of the average radius of pDSGC On and Off dendrites (On: 88.1, STDEV 13.9 μm, Off: 75.9, STDEV 13.7μm, from 25 cells, see Methods) indicates that the spot mostly covered areas beyond the dendritic span of these cells. For each cell tested, we also presented a moving bar stimulus to confirm its directional tuning to posterior-direction motion in the visual field.

The spot stimulus delivered to the pDSGC RF periphery uncovered an asymmetric RF organization where some spots evoked maximal spiking (Max) and other spots presented to the opposite regions (Opp) across the dendritic span evoked minimal responses (**Figures 1B, 1C, S1A, and S1B).** The Max-Opp axis largely corresponds with the preferred-null motion axis, which is shown by the polar plots in Figure 1 where the preferred side is aligned to the top. The preferred side is the side where the preferred direction of motion originates. The majority of the maximum responses to the peripheral spots occurs within 67.5 degrees from the preferred direction of the DSGC and half occur within 22.5 degrees of the preferred direction (**Figures 1B, 1C "Control", and S1A**).

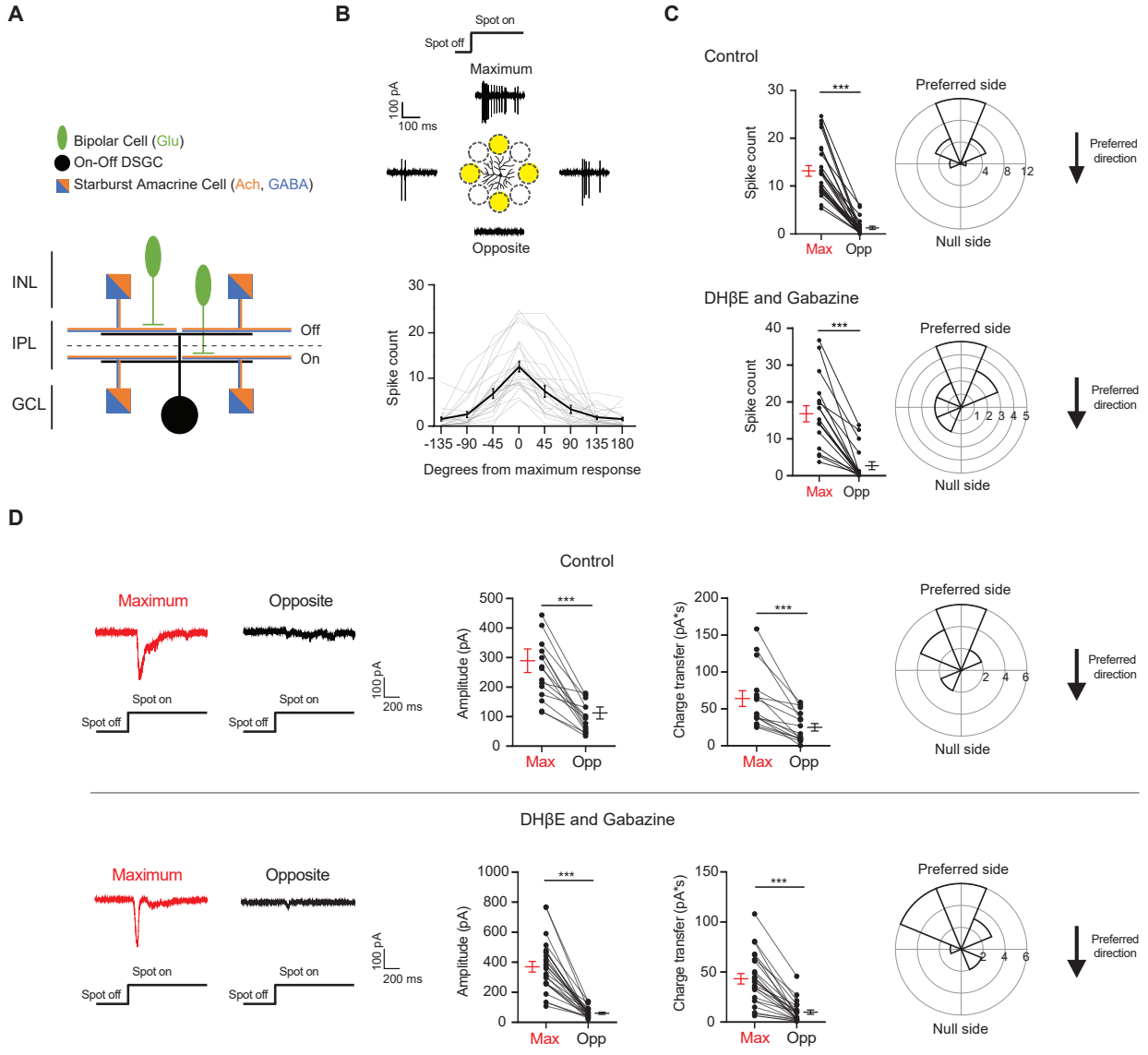

Figure 1. Drd4-GFP labeled pDSGCs have spatially asymmetric glutamatergic receptive fields.

(A) Schematic showing types of presynaptic neurons to an On-Off DSGC and the neurotransmitters they use. **(B)** Top: Example On spiking responses of a pDSGC to four different peripheral spots presented around dendritic span. Bottom: Individual (gray) and mean (black) pDSGC On spike counts evoked by spots presented at different locations (25 cells). **(C)** Top left: Pairwise comparison of mean spike counts in regions evoking the maximum number of On spikes (Max) and the opposite region (Opp) in the control condition (25 cells). Top right: Polar histogram of Max region locations aligned to the preferred-null motion axis. Radius indicates number of cells. Bottom: Same as in top but experiments performed in DHβE + Gabazine (18 cells). **(D)** Left: Example On EPSC responses to spots shown in the regions evoking the strongest EPSCs (Max) and the opposite region (Opp) in control (top) and in DHβE + Gabazine (bottom). Middle: Pairwise comparisons of EPSC amplitude and charge transfer to spots presented in the Max region and Opp region (Control: 15 cells; DHβE + Gabazine: 24 cells). Right: Polar histograms of Max region locations determined by EPSC charge transfer aligned to the preferred-null motion axis. Radius indicates number of cells. Summary statistics are mean ± SEM, ***$p < 0.001$.

Because a well-documented asymmetry in the direction-selective circuit is the asymmetric inhibition from SACs to DSGCs, we next tested whether the displacement of the pDSGC spiking RF is eliminated by blocking SAC inputs. We perfused the retina with the nicotinic antagonist DHβE and the $GABA_A$ receptor antagonist gabazine to block these inputs. Under this condition, we still observed a spatial asymmetry in pDSGC spiking activity evoked by the flashing spots (**Figures 1C, S1A and S1B**, “DHβE and Gabazine”), indicating a spatial displacement of glutamatergic excitation of the pDSGC in the absence of SAC influence.

To directly measure the strength of excitatory inputs to pDSGCs at different stimulus locations, we performed whole-cell voltage clamp recordings of excitatory postsynaptic currents (EPSCs) evoked by peripheral flashing spots. Consistent with the pattern of pDSGC spiking activity, spot-evoked EPSCs show a spatial bias towards the preferred side (**Figures 1D, S1C and S1F**, “Control”). Isolation of the glutamatergic component of the EPSC by the addition of DHβE and gabazine confirms the persistence of the spatial asymmetry, indicating that the glutamatergic excitation of the pDSGC is not isotropic but is spatially displaced relative to the soma (**Figures 1D and S1C – G**, “DHβE and Gabazine”). We noted that gabazine and DHβE reduced the rise and decay time of the EPSC waveform compared to that in the control condition (**Figure S1E**), presumably due to the removal of the cholinergic component of the EPSC. Ablating the GABAergic contribution pharmacologically also rules out the possibility that a strong null-direction GABAergic inhibition is contaminating and artificially reducing the EPSCs on the null side, which is a potential confound during voltage clamp recordings due to imperfect control of membrane potential in distal dendrites (Poleg-Polsky and Diamond, 2011).

Non-uniform excitatory conductance across the preferred-null motion axis contributes to the asymmetric glutamatergic RF

An asymmetric excitatory RF in a retinal neuron may result from asymmetric dendritic arbors and/or an asymmetric distribution of excitatory synaptic inputs across its dendritic field. We performed two-photon imaging of dye-filled dendritic arbors after recording glutamatergic EPSCs evoked by the peripheral flashing spot stimulus described above (**Figures 2A and 2B**). Consistent with previous studies, dendritic arbors of pDSGCs do not exhibit a salient or consistent bias relative to the cell's preferred motion direction. The total dendritic length or the number of dendritic

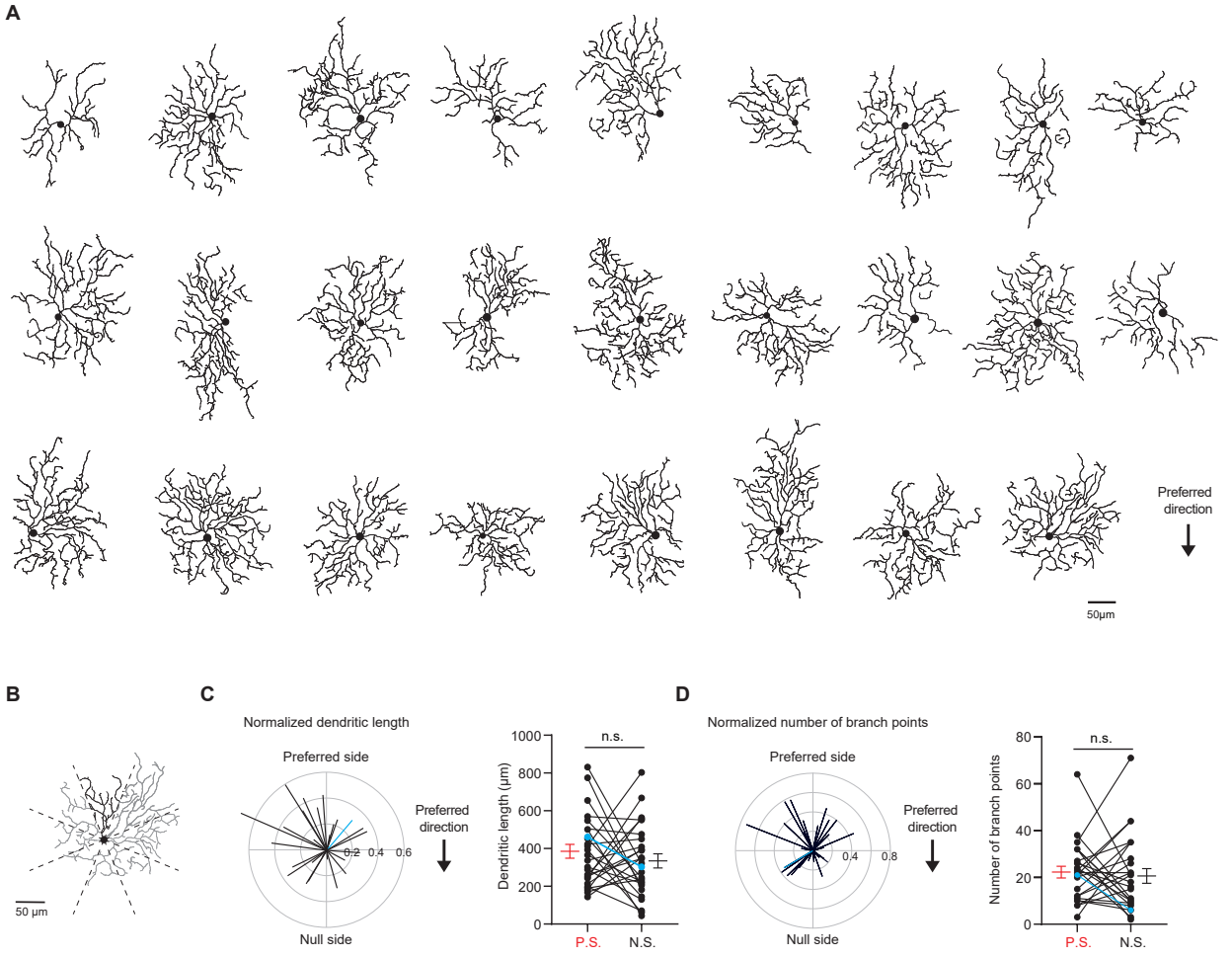

Figure 2. pDSGC dendritic morphology does not show a spatial bias towards the preferred side.

(A) Traced On layer dendritic morphologies of pDSGCs aligned to their preferred-direction motion. **(B)** Example On morphology of a pDSGC cell divided into eight sectors for calculating normalized dendritic length vector. **(C)** Left: Normalized vector sum of On dendritic length aligned to pDSGCs' preferred direction motion. Right: Pairwise comparison of dendritic length on the preferred vs null

198 sides of each cell (26 cells, p = 0.51). Blue represents example cell in **B**. **(D)** Left: Normalized
199 vector sum of On branch points aligned to pDSGCs' preferred direction motion. Right: Pairwise
200 comparison of branch points on the preferred vs null side (26 cells, p = 0.68). Blue represents
201 example cell in **B**. Summary statistics are mean ± SEM.
202
203 branching points does not significantly differ between the preferred and null sides of the
204 pDSGC dendritic field (**Figures 2C, 2D and S2A – C**). This apparent randomness of
205 dendritic arbor distribution relative to the cell's preferred motion direction contrasts with
206 the previously reported mouse On-Off DSGC subtype preferring motion in the superior
207 direction that have dendritic arbors strongly displaced to the null side of the soma (El-
208 Quessny et al., 2020; Kay et al., 2011; Trenholm et al., 2011).
209
210 The preferred motion direction of the pDSGC spiking activity is shaped by the
211 interaction of its excitatory and inhibitory inputs. Next, we examined the relationship
212 between pDSGC dendritic morphology and its glutamatergic inputs. We found a non-
213 random skew of the pDSGC dendritic length and number of branch points towards the
214 regions corresponding to spots evoking the strongest glutamatergic EPSCs (**Figure**
215 **S2D and S2E**). However, the extent of the dendritic bias is not correlated with the
216 extent of the bias in EPSC strength (**Figure S2F**), suggesting that dendritic arbor
217 density alone cannot fully explain the displacement of the pDSGC glutamatergic RF.
218
219 To further explore the relationship between the pDSGC glutamatergic RF and its
220 dendritic distribution, we performed another set of experiments to obtain a more
221 complete RF map. First, the preferred direction of each cell's spiking activity was
222 determined by loose cell-attached recordings using a moving bar stimulus with no
223 synaptic blockers. Next, peripheral flashing spots were used to estimate the spatial
224 displacement of the pDSGC glutamatergic RF in the presence of nicotinic and
225 GABAergic receptor antagonists (DHβE + Gabazine) as described above. Then, a
226 smaller, 20 μm diameter bright stationary spot was repeatedly flashed at random
227 locations within a 11-by-11 220 μm square grid centered on the pDSGC soma. A
228 heatmap of glutamatergic EPSC charge transfer evoked by the small flashing spot was
229 generated and overlaid with the reconstructed dendritic arbors for each pDSGC (**Figure**
230 **3A**).
231
232 RF mapping with small flashing spots revealed a spatial displacement of
233 glutamatergic EPSC distribution that aligns well with the displacement determined by
234 larger spots presented to the pDSGC periphery (**Figure 3B**). Similar to the
235 displacement pattern revealed by stimulation of the RF periphery, the strongest
236 glutamatergic EPSCs are preferentially located on the preferred side of pDSGC somas
237 (**Figure 3C**). Notably, for most cells, the center of the glutamatergic EPSC RF is
238 displaced from the center of the dendritic field (**Figure S3A and S3B**), indicating

additional mechanisms underlying the glutamatergic RF displacement apart from the dendritic arbor distribution.

We further examined the strength of the glutamatergic input across the pDSGC dendritic field (**Figure 3D**). We normalized the EPSC charge transfer by the total

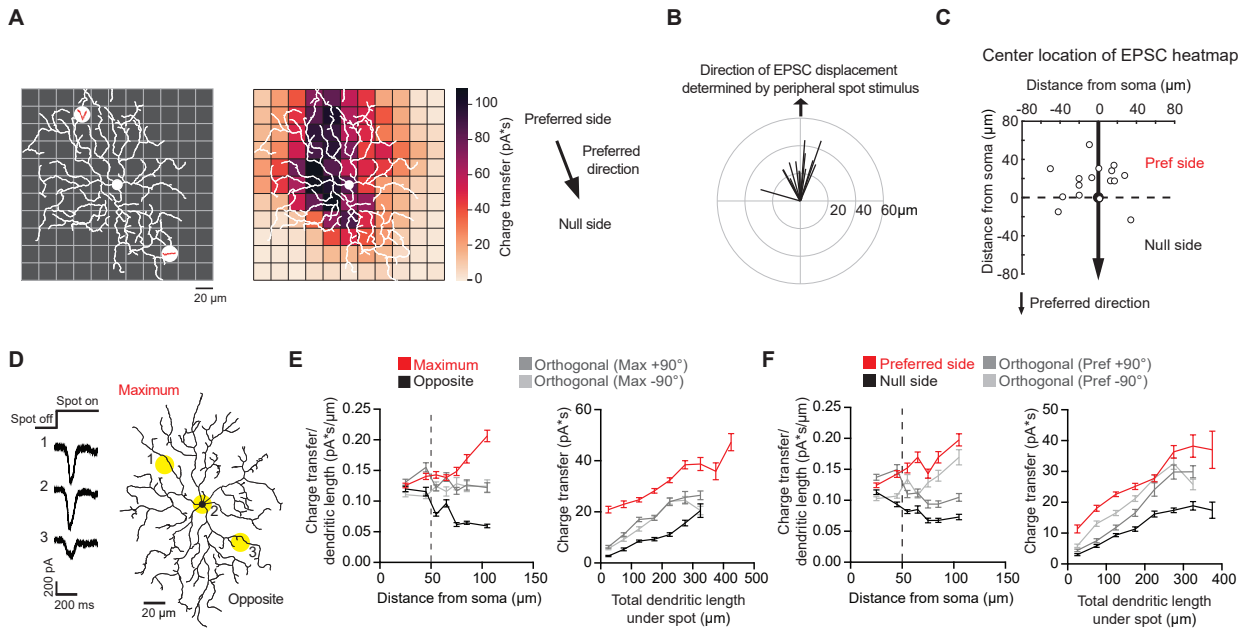

Figure 3. Non-uniform glutamatergic synaptic excitation across pDSGC dendritic span contributes to skewed excitatory receptive field.
(A) Left: Schematic for small spot RF mapping experiment in DHβE + Gabazine. Middle: Example heat map. Right: Preferred motion direction of the example cell in relation to the preferred side and the null side of the cell's RF. **(B)** Vector sum plot of On EPSC charge transfer center of mass determined by small spot RF mapping aligned to the region where a peripheral spot evokes the maximum glutamatergic EPSC (upward arrow). **(C)** Spatial locations showing centers of mass of glutamatergic excitatory On charge transfer obtained from experiments illustrated in **A** aligned to each cell's preferred motion direction (15 cells). **(D)** Example On EPSC responses to spots presented to a pDSGC along the maximum-opposite axis of glutamatergic RF displacement. **(E)** Left: On "EPSC current density" (i.e. ratio of charge transfer per dendritic length) versus distance from soma along the maximum-opposite axis of glutamatergic RF displacement (16 cells, ***$p < 0.001$) as well as along the orthogonal axis. Right: Summary plot of glutamatergic charge transfer as a function of total dendritic length centered around the flashing spot for spots shown more than 50 µm away from the soma (16 cells, ***$p < 0.001$). **(F)** Same as **E** but along the preferred-null motion axis (15 cells, charge transfer/dendritic length vs distance from soma **$p = 0.0026$, charge transfer vs dendritic length ***$p < 0.001$). Summary statistics are mean ± SEM.

267 dendritic length in a circle with a 60 μm diameter centered on each small flashing spot.
268 This provides an estimate of the strength of glutamatergic inputs per unit dendritic
269 length, or "EPSC density", at each stimulus location. When we calculated the density
270 along the axis of maximal glutamatergic RF displacement, we found that the EPSC
271 density on the displaced side of the dendritic field is larger than the corresponding
272 region on the opposite side (**Figures 3E**, left, and **S3E**). From 50 μm away from the
273 soma, spots on the side corresponding to the maximum displacement (Maximum) yield
274 stronger EPSCs than spots on the opposite side (Opposite), while controlling for the
275 same dendritic length (**Figures 3E,** right, and **S3E**). This heterogeneity in EPSC density
276 across the dendritic span persists when comparing EPSC responses along the
277 preferred-direction motion axis of the cell (**Figures 3F and S3F**). Analysis of the peak
278 amplitudes showed similar results as charge transfer (**Figures S3C and S3D**).
279
280 Next, we asked what mechanisms could underlie the non-uniform excitatory
281 conductance across the dendritic span. Because bipolar cells provide the dominant
282 excitatory input to DSGCs, the enhanced excitation on the preferred side of the
283 receptive field could stem from increased density or strength of bipolar synapses. Using
284 a published serial block-face scanning electron microscopic (SBEM) dataset of the adult
285 mouse retina (Ding et al., 2016), we reconstructed large numbers of ON starburst
286 amacrine cells and On-OFF DSGCs (**Figures 4A**). The preferred direction of the traced
287 DSGCs was inferred from the mean orientation of starburst dendrites making
288 'wraparound' synapses onto the DSGCs, following the previous work of Briggman et al.
289 (Briggman et al., 2011) (**Figure 4B**). Among all DSGCs, four preferred directions were
290 seen roughly 90 degrees apart, as expected for most retinal locations (Sabbah et al.,
291 2017). We selected three On-Off DSGCs for which the inferred preferred direction of
292 motion fell on the horizontal axis like the cells we studied electrophysiologically, two with
293 one motion preference, and the other with the opposite preference. Technical
294 constraints prevented us from saying which cells preferred posterior motion and which
295 cells preferred anterior motion (see Methods). We then mapped the distribution of
296 bipolar ribbon synapses onto the dendrites of these three cells. We found no marked
297 gradient in ribbon density across the preferred-null motion axis of the three cells
298 (**Figures 4D – 4F, S4A – S4B),** suggesting that the gradient in EPSC density across
299 this axis is not determined by the density of bipolar inputs.
300
301 In addition to ribbon density, we also examined the time course of glutamatergic
302 EPSCs in the presence of DHβE and gabazine along the axis of maximal glutamatergic
303 RF displacement and along the preferred-null motion axis. We found no significant
304 differences in the latency, rise and decay times in EPSC waveforms across the axis of
305 maximal glutamatergic RF displacement in response to the small flashing spots
306 (**Figures 4G – 4I,** left panels). In addition, we did not detect a monotonic change in
307 glutamatergic EPSC kinetics along the preferred-null motion axis in DHβE and

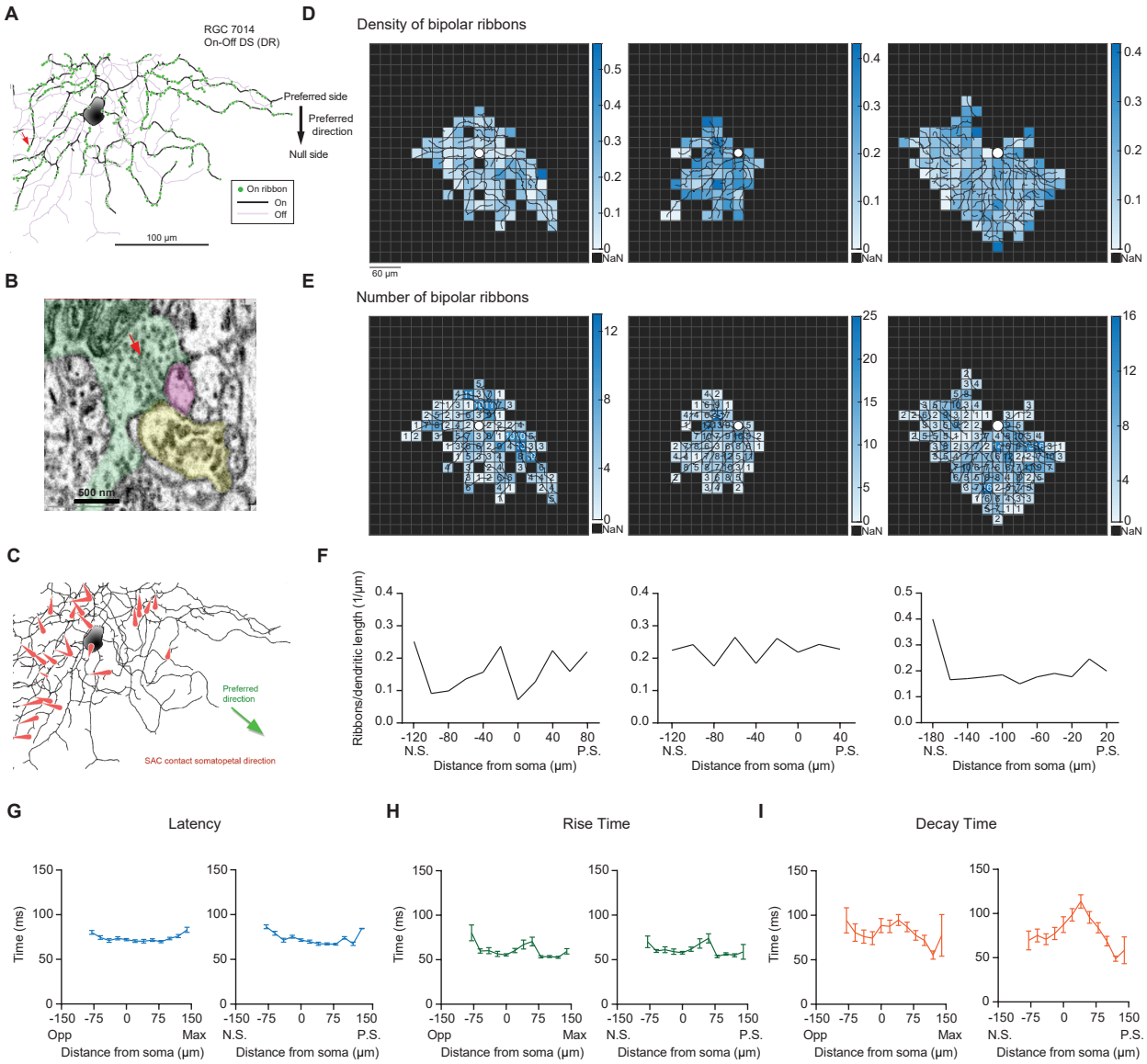

Figure 4. Neither the density of bipolar ribbon inputs nor the kinetics of glutamatergic EPSCs varies systematically along the axis of RF displacement.

(A) Top: Distribution of ribbon synaptic input to one of the three reconstructed On-Off DSGCs. **(B)** Ultrastructure of the synapse indicated by the red arrow in **A**, as visualized by serial block-face electron microscopy. The presynaptic bipolar cell (green) belongs to Type 5t. Red arrow marks the ribbon. The magenta profile belongs to the On-Off DSGC. The other postsynaptic partner at this dyad synapse was another ganglion cell (yellow). Though only a fragment was included in the volume, it was presumably a DSGC, since it costratified entirely with the inner dendrites of the On-Off DSGC (**A**; black dendrites). **(C)** SAC inputs onto example On-Off DSGC. Red arrows indicate the direction and location of the SAC inputs on the DSGC dendrites. **(D)** Density map of bipolar ribbon synapses for 3 example On-Off DSGCs with estimated preferred directions along the posterior-anterior axis (see Methods). The soma location is indicated by the white spot in the center. **(E)** Bipolar ribbon heat map for the 3 example cells, respectively. The number of ribbons in each square are indicated. **(F)** Quantification of ribbon density across the preferred-null axis, respectively. The soma location is at 0.

(N.S. = null side, P.S. = preferred side). **(G)** Left: Summary of latency of glutamatergic EPSC responses along the maximum-opposite axis (Max = maximum glutamatergic EPSC region, Opp = opposite region)(16 cells, p = 0.75). Right: Summary of latency along the preferred-null motion axis (N.S. = null side, P.S. = preferred side)(16 cells, p = 0.88). **(H)** Same as in **G**, except for rise time (10% - 90%). (Left: p = 0.12, right: p = 0.21, 16 cells). **(I)** Same as in **G**, except for decay time (90% - 30%). (Left: p = 0.25, right: p = 0.26, 16 cells). Summary statistics are mean ± SEM.

gabazine (**Figures 4G – 4I,** right panels) or in DHβE only (**Figures S4C and S4D**). That we find no differences in the kinetics of EPSC waveforms across the pDSGC dendritic field contrasts with a previous study of On DSGCs reporting a gradient of EPSC kinetics from slow/sustained to fast/transient along the preferred-null motion axis (Matsumoto et al., 2019). This gradient in On DSGC EPSC kinetics is thought to arise from different bipolar cell subtypes, and may implement a Hassenstein-Reichardt-Detector-like mechanism for the On DSGCs' direction selectivity. Thus, our data suggest that there are no marked differences in the subtypes of bipolar inputs along the preferred-null axis of On-Off pDSGCs.

Null-direction response emerges during partial activation of the displaced pDSGC RF

Because On-Off DSGCs are thought to be dedicated to encoding object motion, we next asked how the displaced excitatory RF of the pDSGC revealed by the stationary flashing stimuli contributes to motion processing. We reasoned that because conventional simple motion stimuli such as moving bars and drifting gratings traverse the entire RF of the pDSGC, SAC-mediated inhibition would exert a dominant influence on pDSGC spiking by strongly suppressing the pDSGC null-direction response. However, when motion trajectories are more complex, as often occurs in the natural environment, the displaced excitatory pDSGC RF may confer additional characteristics to the cell's motion encoding. Therefore, we investigated how the direction-selective circuit would process interrupted motion because moving objects in the natural environment often pass behind occluders or start moving from behind other objects.

To examine if the displaced excitatory RF of the pDSGC plays a role in encoding interrupted motion, we created an occluded motion stimulus where a moving bar disappeared behind a central occluder 220 μm in diameter (**Figure 5A**). The occluder covered the dendritic span of the pDSGC and a substantial portion of its RF center. In contrast to the full-field motion stimuli, the occluded motion stimulus caused both preferred and null-direction spiking responses (**Figures 5B, S5A – S5C**). These responses are only evoked when the bar travels in the preferred side, which corresponds to the displaced side of the pDSGC RF (**Figure 5B**, middle row, **5C, S5B**

365 **and S5C**). In contrast, no spiking response is evoked when the bar moves across to the
366 null side beyond the occluder (**Figures 5B,** bottom row, **5C, S5B and S5C**). To test
367 whether this regional difference is due to the asymmetric wiring between SACs and
368 DSGCs, we blocked the cholinergic and GABAergic transmission with DHβE and
369 gabazine and saw that the regional difference persisted (**Figures 5C and S5B**).
370 Consistent with the spiking pattern, the EPSC responses also reflected this regional
371 asymmetry (**Figure 5D**). In contrast, IPSC responses to the occluded bar stimulus are
372 displaced to the opposite side compared to EPSC responses (**Figure S5D**), consistent
373 with the asymmetric wiring pattern from SACs from the null side to the DSGC (Briggman
374 et al., 2011; Fried et al., 2002; Lee and Zhou, 2010; Wei et al., 2011; Yonehara et al.,
375 2011).
376

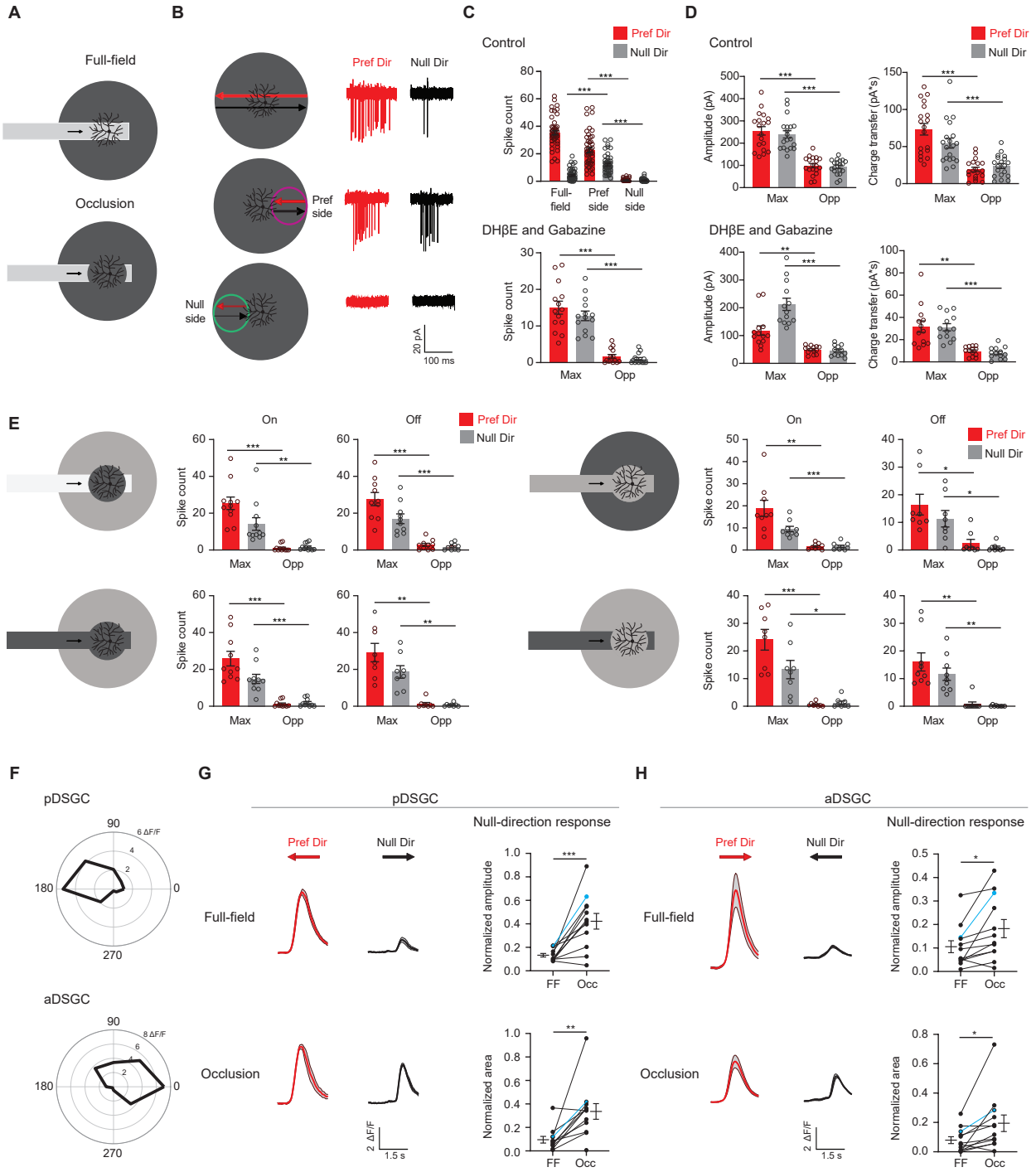

Figure 5. Displaced excitatory receptive field contributes to null-direction responses in the preferred region.

(A) Full-field moving bar and occluded bar stimuli. **(B)** Example On spiking responses of a pDSGC to full-field bar (top) and occluded bar stimulus (middle, bottom) moving in the preferred (red) and null (black) directions. **(C)** Top: Mean spike counts of pDSGCs to the full-field moving bar (full-field) and the occluded moving bar on the preferred side and null side (48 cells). Bottom: Mean

385 spike counts in DHβE + Gabazine to the occluded bar stimulus in the region evoking the maximum
386 spiking (Max) and the opposite region (Opp) (13 cells). **(D)** Mean pDSGC EPSC peak amplitude
387 and charge transfer in the region evoking the maximum response (Max) and the opposite region
388 (Opp) in the control (top, 19 cells) and DHβE + Gabazine (bottom, 13 cells) conditions. (In DHβE
389 + Gabazine: Pref Dir – Max vs Pref Dir – Opp amplitude **p = 0.0028, Pref Dir – Max vs Pref Dir
390 – Opp charge transfer **p = 0.0012). **(E)** Mean On and Off spiking responses to occluded bar
391 stimulus at different contrast configurations. Top left: On: 11 cells, Max null dir. Vs Opp null dir.
392 **p = 0.008. Off: 10 cells. Bottom left: On: 10 cells. Off: 8 cells. Top right: On: 9 cells, Max pref.
393 dir. Vs. Opp pref. dir. **p = 0.003. Off: 8 cells, Max pref. dir. Vs Opp. Pref. dir. *p = 0.034, Max
394 null dir. Vs Opp null dir. *p = 0.02. Bottom right: On: 8 cells, Max null dir vs Opp null dir. *p =
395 0.014. Off: 9 cells, Max pref. dir. Vs Opp pref. dir. **p = 0.004, Max null dir. Vs Opp null dir. **p =
396 0.002. **(F)** Top: Example directional tuning curve of GCaMP6 signal of a pDSGC. Bottom:
397 Example tuning curve of an aDSGC. **(G)** Top left: Example GCaMP6 fluorescence traces of a
398 pDSGC for the full-field moving bar in the preferred (red) and null (black) directions. Bottom left:
399 Example GCaMP6 traces of the cell for the occluded bar stimulus. Shaded areas represent SEM.
400 Top right: Normalized amplitude of the posterior-preferring cell null-direction response during the
401 full-field bar and the occluded bar (12 cells). Bottom right: Normalized area of the null-direction
402 response during the full-field bar and the occluded bar (12 cells, **p = 0.0035). **(H)** same as in **G**,
403 except for aDSGCs. (12 cells, normalized amplitude *p = 0.013, normalized area *p = 0.019).
404 Summary statistics are mean ± SEM, ***p < 0.001 except where specified otherwise.
405
406 Moreover, we blocked $GABA_C$ receptor activity, glycine receptor activity, and gap-
407 junction coupling with TPMPA, strychnine, MFA, and Carbenoxolone, respectively, and
408 found that the spatial asymmetry of the spike response remains during the occluded
409 motion stimulus (**Figures S5H – S5K**). Based on these pharmacology results, we
410 conclude that the asymmetric glutamatergic RF of the pDSGC contributes to robust
411 spiking in both null and preferred directions when the preferred side of the RF is
412 activated by the occluded motion stimulus.
413
414 Since there are two On-Off DSGC subtypes that are tuned to the opposite
415 directions along the posterior-anterior axis, we investigated if the anterior-direction-
416 selective DSGC (aDSGC) exhibits the same null-direction response pattern to the
417 occluded motion stimulus as the pDSGC. To identify both DSGC subtypes, we
418 performed calcium imaging of GCaMP6-expressing RGCs in another transgenic mouse
419 line carrying Vglut2-IRES-Cre and floxed GCaMP6f (**Figure S6A**) during the full-field
420 moving bar stimulus. We then used an online analysis to identify aDSGCs and pDSGCs
421 based on the directional tuning of their calcium signals to the anterior and posterior
422 motion directions (**Figures 5F and S6B – C**). Next, we centered the occluded motion
423 stimulus on individual aDSGC and pDSGC somas and performed calcium imaging
424 during the occluded motion stimulus. Consistent with pDSGC spiking activity, a
425 significant null-direction calcium response of the pDSGCs was evoked when the
426 occluded moving bar traveled across the receptive field to the preferred side of the RF

(**Figures 5G and S6D**). Notably, aDSGCs also exhibited a null-direction response to the occluded motion stimulus that is similar to that of pDSGCs (**Figure 5H and S6D**), indicating that aDSGC RFs are also displaced to the preferred side.

The above results show that continuous motion interrupted by a stationary occluder in the center of the pDSGC's RF causes unexpected null-direction spiking as the bar emerges from behind the occluder into the preferred side of the pDSGC RF. However, this occluded motion stimulus cannot distinguish whether the interruption itself or only the start position of the emerging bar was necessary for the null-direction response. Therefore, we created a stimulus where a bar emerges at different locations along the preferred-null motion axis of the cell. The start motion of the bar activates different parts of the DSGC's receptive field (Figure 6A). For the null-direction moving bar, there is an increase in both the spike number and the firing rate as the starting position of the moving bar is located past the soma on the preferred side of the pDSGC RF (**Figures 6A – 6C**). Thus, the emergent growing edge caused null-direction spiking of pDSGCs in a similar pattern as the moving bar emerging behind the central occluder. These results illustrate that the null-direction response of the pDSGC during the occluded motion stimulus is dependent on the position in the receptive field from which the moving edge emerges, not the previous motion approaching the occluder.

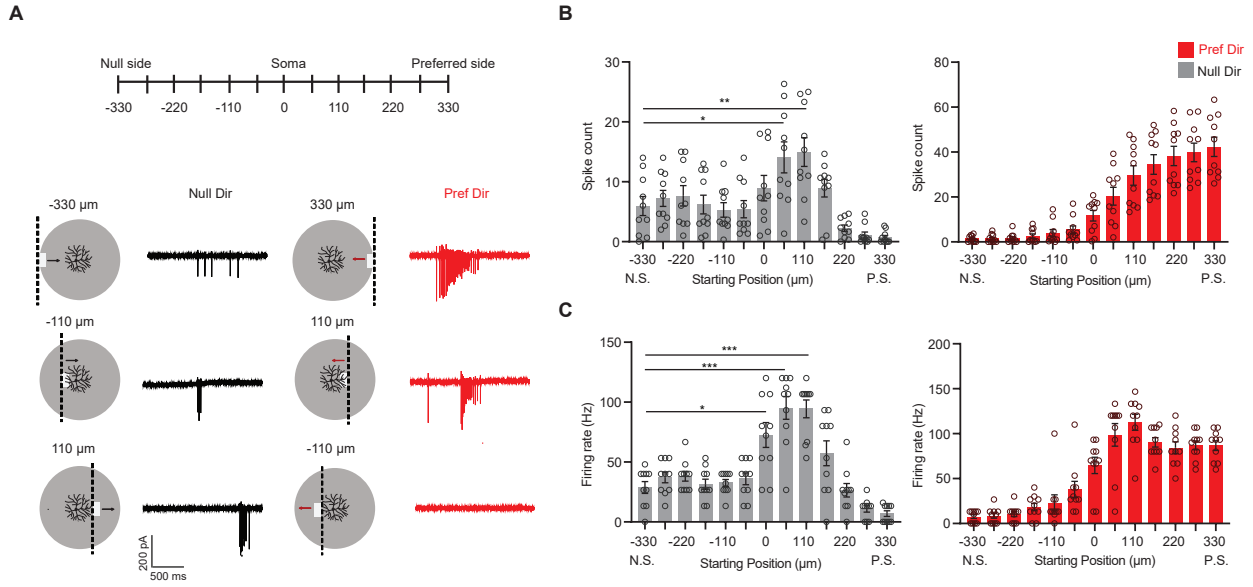

Figure 6. Null-direction response is dependent on start position of emerging bar. **(A)** Schematic of moving bars emerging from different locations along the DSGC's preferred-null motion axis and example spiking responses. The soma location is at 0. Vertical dashed lines on the schematic indicate the positions of the emerging leading edge of the moving bar. **(B)** Mean spike counts (null direction: -330 vs 55 *p = 0.012, -330 vs 110 **p = 0.0088) and **(C)** firing rates

454 (null direction: -330 vs 0 *p = 0.014) to bars emerging from different locations along the preferred-
455 null motion axis (10 cells). Summary statistics are mean ± SEM, ***p < 0.001 except where
456 specified otherwise.
457
458
459 **Null-direction responses of DSGCs during partial activation of their RFs can be**
460 **useful for decoding object location**
461
462 We explored how the displaced RFs could functionally benefit the computations
463 performed by pDSGCs. First, we considered whether a displaced excitatory RF could
464 benefit the direction-selective mechanisms during full-field smooth motion. By
465 comparing the onset times of EPSCs and IPSCs to preferred-direction motion, we found
466 that cells with more spatially separated excitatory and inhibitory receptive fields were
467 more direction-selective (**Supplemental Figure 7M**).
468
469 Next, we considered scenarios when the displaced RF is partially activated by
470 moving stimuli. Our experimental results show that pDSGCs generate robust spiking
471 activity in both the preferred and null directions when a moving object appears and
472 starts moving on the preferred side of the cell's RF, as when an object emerges from
473 behind an occluder positioned over the cell's soma. We asked whether this prima facie
474 aberrant signaling can have a functional role relevant to the behavioral goals of the
475 organism.
476 We hypothesize that partial RF activation of a DSGC at a narrow region in visual
477 space may provide precise information about the spatial position of a moving object
478 along an interrupted motion trajectory. In particular, if a moving object emerging from
479 behind an occluder activates the preferred side of an On-Off DSGC's RF, this DSGC
480 would generate a null-direction spiking response together with the preferred-direction
481 response of a nearby On-Off DSGC subtype preferring the opposite motion direction
482 (**Figure 7A**). Such synchronous spiking activity between DSGCs of opposite preferred
483 directions at the location of the occluder could yield a stronger and more localized
484 spatial signal at the population level in response to interrupted motion.
485
486 To test how the null-direction response during interrupted motion might enhance
487 downstream estimation of stimulus position, we simulated the spiking responses of
488 pDSGCs in a population model consisting of On-Off DSGC subtypes that prefer
489 opposite motion directions on the posterior-anterior axis (aDSGCs and pDSGCs, **Figure**
490 **7A**). One thousand cells of each subtype were arranged in a two-dimensional array with
491 biologically realistic positional jitter, such that the spatial positions of the two subtypes
492 were uncorrelated. We simulated a bright edge moving along the posterior-anterior axis
493 in a single direction at a constant velocity under both uninterrupted and interrupted
494 motion conditions and analyzed the On response to the edge. The mean spiking

495 response of each DSGC was modeled as a rectified sine wave with parameters
496 obtained from our experimental data, and sub-Poisson trial-to-trial variability was
497 introduced to the mean spiking response on each trial (**Figure S7**). The spatial positions
498 of the DSGCs were shuffled in each simulation block to allow us to sample different
499 spatial arrangements of the RFs.
500
501 Using a labeled-line decoder (see Methods), we compared the scenario in which
502 none of the DSGCs were occluded (full-field) with the scenario in which a single
503 occluder was placed near the center of the population. Our modeling results show that
504 the null-direction response degrades the population estimate of the motion direction as
505 would be expected (**Figure 7D**), but that the coincidence of the null-direction response
506 from pDSGCs and the preferred-direction response of neighboring aDSGCs when the
507 bar exits the occlusion substantially improves the estimation of bar position (**Figure 7C**).
508 For a bar traveling at the speed of 330 μm /sec (the lowest speed in our experiments
509 and simulations), the synchronous firing between pDSGCs and the neighboring
510 aDSGCs reduces the error in the population estimate of the bar edge's spatial position
511 by over 80 percent. This reduction in error is present, albeit smaller, even at higher
512 speeds. At the highest speed of 2640 μm /sec, there was still around a 40 percent
513 decrease in position estimation error during the occlusion trials. The absolute position
514 error decrease was around 3 degrees of visual angle across bar speeds in models with
515 low levels of background noise.
516 Because the displaced excitatory receptive field also induced differential firing
517 responses to stationary spots presented outside of the cell's dendritic field (**Figure 1**),
518 we asked whether the displacement was useful for detecting non-directional contrast
519 changes for a small stationary spot. Receptive field mapping experiments showed that
520 the spiking receptive field is displaced towards the preferred side. However, the total
521 diameter of the asymmetric receptive field is around 220 μm, which is larger than the
522 average dendritic span of pDSGCs (**Figure S1H**). We analyzed whether a displaced
523 receptive field would benefit the position estimation using non-directional contrast
524 change signals. We found that the accuracy of estimating position from contrast
525 changes is the same for populations with asymmetric receptive fields and populations
526 with symmetric receptive fields. The detection of the contrast change would only
527 improve if the receptive field size decreased (data not shown). Directed motion is
528 required for an improvement in position estimation because a null-direction signal can
529 only occur in a small region on the preferred side. Therefore, the synchrony of the null-
530 direction and preferred-direction signals within the population yields a more spatially
531 constrained signal necessary for fine spatial discrimination of moving stimuli.
532
533 The synchronous firing may, itself, also be a useful alarm signal that triggers
534 processing downstream of the retina, independent of the precise position information it

535 might additionally convey. To investigate whether the synchronous firing during
536 occlusion trials can be read out from a population response, we utilized a coincidence
537 decoder to determine whether full-field motion trials can be distinguished from occluded
538 motion trials. A filter was fit to the null-direction spiking response from the occlusion
539 trials (**Figure 7E**), and when the convolution of the firing rate with the filter rose above a
540 threshold level **(Figure 7F)**, the detector would identify an occlusion trial.
541
542 Evaluating the decoder performance showed that the decoder is highly
543 successful at identifying occlusion trials in conditions with low background firing rates. In
544 conditions with background firing rates of 10 Hz or less, the decoder correctly identified
545 occlusion trials with more than 99% accuracy (**Figure 7G**). This coincidence detection
546 model suggests that the synchrony of preferred-direction responses from one DSGC
547 subtype and the null-direction responses from the opposite DSGC subtype during
548 interrupted motion conditions can be easily detected. This salient synchrony signal can
549 potentially inform downstream visual areas of the type of motion that is occurring or
550 provide an alarm signal to the animal that there is an unexpected change in their
551 environment.
552

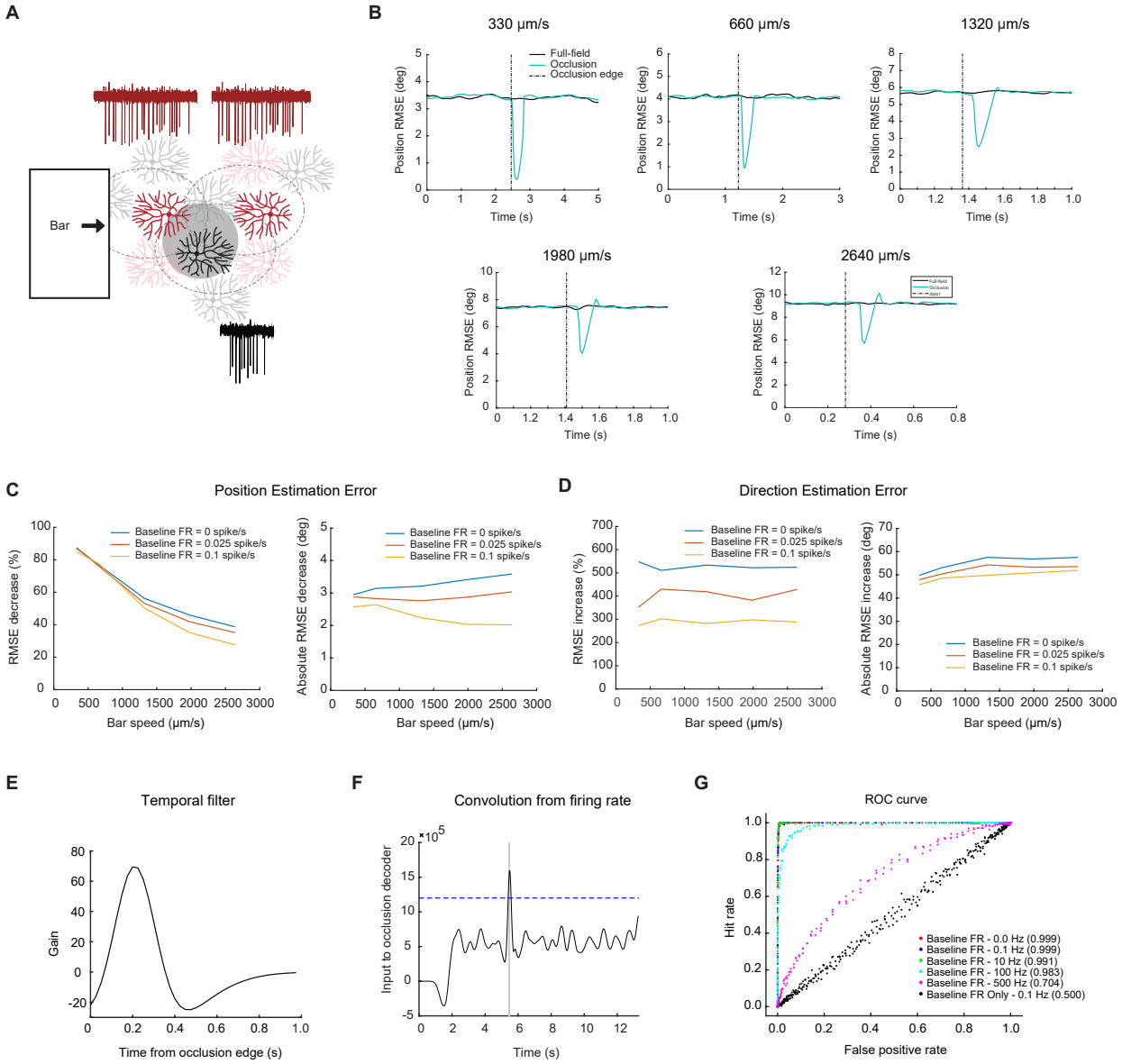

Figure 7. Null-direction spiking of On-Off DSGCs during the occluded motion stimulus improves position estimation.

(A) Schematic of the DSGC population model along with example spike trains for two pDSGCs (red trace showing their preferred-direction responses) and an aDSGC (black trace showing its null-direction response). An occluder 220 μm wide (shaded circle) was placed near the middle of the population. **(B)** Example root-mean-square error in estimating the position of the light bar's leading edge for full-field (black) and occluded (blue) motion across different bar speeds. **(C)** Left: Position error percent decrease across speeds. Right: Absolute error decrease across bar speeds. **(D)** Same as in **C**, but for direction estimation error. **(E)** Temporal filter for detecting occlusion response. **(F)** Convolution of firing rate from the temporal filter. Dashed line represents example threshold. **(G)** ROC curve with different levels of baseline firing for a bar of speed 330 μm/sec. Legend shows performance level of decoder for each level of baseline firing.

Discussion

Our study reveals a new form of asymmetry in the direction-selective circuit: a spatial displacement of glutamatergic inputs to the preferred side of the On-Off pDSGCs due to a non-uniform distribution of synaptic conductances across the pDSGC dendritic span. The impact of this displaced excitation on DSGC spiking is demonstrated by using moving stimuli with interrupted trajectories, a feature abundant in natural scenes. In contrast to full-field continuous motion which maximizes the contribution of SAC-mediated null-direction inhibition, occluded motion stimuli reduce the contribution of SAC-mediated inputs to allow the excitatory receptive field to dominate the spiking response in a non-directional manner when only part of the RF is stimulated. Therefore, an On-Off DSGC's response to occluded motion stimuli is determined both by how much of the receptive field is activated and where that activation occurs.

The non-isotropic excitation of the pDSGC alludes to a more sophisticated set of wiring and signaling mechanisms from the bipolar cell population (Franke et al., 2017). A detailed explanation of the glutamatergic RF displacement awaits future studies. The gradient of glutamatergic current density across the pDSGC dendritic span may arise from a number of possible scenarios including varying strengths of individual glutamatergic synapses, heterogeneous membrane properties across pDSGC dendritic field, and contribution from Vglut3+ amacrine cells (Kim et al., 2015; Lee et al., 2016).

It is intriguing to speculate how the displaced excitatory receptive field properties of On-Off DSGCs can influence downstream computation. Previous theoretical analysis has addressed the encoding of motion direction by DSGCs at the population level (Fiscella et al., 2015; Zylberberg et al., 2016). In this study, we explored a hypothesis that On-Off DSGC population activity contains information about both the direction and the location of a moving object. When motion trajectories are not continuous, the null-direction responses from cells near the occlusion edge improves the encoding of location at the expense of direction encoding. We speculate that the trade-off between positional and directional encoding, which occurs when an object emerges from behind anther object, may reflect the animal's greater need for positional information of the emerging object than the direction in which it is moving. Additionally, the synchronous response of null-direction and preferred-direction spiking can potentially provide a salient alarm signal for discontinuous motion, which may help the animal quickly attend to the site of the change. Considering the population activity of multiple subtypes of On-Off DSGCs after an interruption in the motion allows for the encoding of more information than motion direction. Our findings that the population activity across cell types can help resolve ambiguities in single cell responses share a common theme with previous modeling experiments from Kühn and Gollisch (2019), which show that multiple DSGCs subtypes with different motion direction tuning in the salamander retina are needed to isolate motion-related information from confounding contrast signals under complex texture motion. Our current investigation adds to the accumulating

evidence that retinal population activity across multiple subtypes enhances decoding of visual features from ambiguous, multiplexed signals.

In contrast to the On DSGC that encodes global motion during optic flow and participates in the optokinetic reflex, On-Off DSGCs are considered encoders of local motion, and project to the superficial layer of the superior colliculus (SC) and the shell region of the dorsal lateral geniculate nucleus (dLGN) (Cruz- Martín et al., 2014; Huberman et al., 2009; Rivlin-Etzion et al., 2011). In the SC, On-Off DSGC inputs give rise to the direction selectivity of postsynaptic collicular neurons (Shi et al., 2017), indicating that these collicular neurons do not receive retinal inputs from a broad range of RGC types, but specifically from On-Off DSGCs. Since the superficial layer of the SC is well recognized for its roles in encoding spatial locations and instructing stimulus-directed defensive and prey behaviors (Basso et al., 2021), the encoding of the spatial location of an emerging moving object by On-Off DSGCs may benefit rapid sensorimotor decisions that involve collicular circuitry.

It is likely that other ganglion cell types also participate in fine spatial discrimination. For example, certain types of small receptive field RGCs such as W3 RGCs and HD-RGCs may also be well-suited encode object location (Jacoby et al., 2017; Kim et al., 2010; Zhang et al., 2012). It is worth noting that W3 RGCs are activated only in specific instances where the background is completely uniform, whereas On-Off DSGCs can be activated in a wide range of visual environments, including environments with noisy backgrounds (Chen et al., 2017; Chen et al., 2020). HD-RGCs also have small receptive fields, and computational modeling experiments have shown that the errors in object location between On-Off DSGCs after motion interruption and HD-RGCs are very similar in scale (Jacoby et al., 2017). However, given the divergent and type-specific central projection patterns of mouse ganglion cell types (Martersteck et al., 2017), the position information encoded by other position encoders such as W3 and HD-RGCs may not be available to the specific downstream circuits that receive On-Off DSGC inputs. Our modeling study suggests that the population response of On-Off DSGCs after a motion interruption helps On-Off RGCs achieve the same performance as other ganglion cell populations implicated in fine spatial discrimination.

Given the many outstanding questions on the retinorecipient circuitry, On-Off DSGCs may participate in different visual processing tasks compared to other ganglion cell types by projecting to different areas for implementing different responses (Kay et al., 2011; Sanes and Masland, 2015). Or, they could provide complementary information about the spatial location of moving objects when considered with other RGC populations. In either scenario, our theoretical analysis indicates that the information of spatial location is contained within the On-Off DSGC population response, and that it is possible that higher visual centers stand to benefit from this information. Ultimately, elucidating the roles of diverse RGC types in motion encoding requires a thorough understanding of visual signal transformations along the processing pathways and how the visual system instructs visually guided behavior.

Acknowledgements

We thank Chen Zhang for managing the mouse colony and Dr. John Maunsell, Dr. Siwei Wang, Mathew Summers, Malak El-Quessny, and Benjamin Hoshal for advice on the manuscript. This work was supported by NIH R01 EY024016 and the McKnight Scholarship Award to W. W., the NSF GRFP DGE-1746045 to J.D., NIH F31 EY029156 to H.E.A., the NSF Career Award 1652617 and the Physics of Biological Function PHY-1734030 to S.E.P., and NIH RO1 EY012793 to D.B.

Competing Interests

All authors would like to report no competing interests.

Methods

Animals

Chat-IRES-Cre mice (129S6-Chat$^{tm2(cre)Lowl}$/J) and floxed *tdTomato* mice (129S6-*Gt(ROSA)26Sor*$^{tm9(CAG\text{-}tdTomato)Hze}$/J) were acquired from the Jackson Laboratory. *Drd4-GFP* mice were originally developed by MMRRC (http://www.mmrrc.org/strains/231/0231.html) and were backcrossed to the C57BL/6 background. These lines were crossed so that both pDSGCs and SACs were labeled. *Vglut2-IRES-Cre* mice and floxed *Ai95(RCL-GCaMP6f)-D* mice were acquired from Jackson Laboratory and were crossed and used for calcium imaging experiments. Mice of ages P21 – P60 of either sex were used. All procedures regarding the use of mice were in accordance with the University of Chicago Institutional Animal Care and Use Committee and with the NIH Guide for the Care and Use of Laboratory Animals and the Public Health Service Policy.

Whole-mount retina preparation

Mice were dark adapted for 1 hour and then were anesthetized with isoflurane and euthanized by decapitation. Retinas were isolated at room temperature in oxygenated Ames' medium (Sigma-Aldrich, St. Louis, MO) under infrared illumination. The retinas were separated into dorsal and ventral halves and were mounted ganglion-cell-layer up on top of a ~1.5 mm^2 hole in a small piece of filter paper (Millipore, Billerica, MA). The orientation of the posterior, anterior, inferior, and superior directions were noted for each piece. During the experimental day, the mounted retinas were kept in darkness at room temperature in Ames' medium bubbled with 95% O_2/ 5% CO_2 until use (0 – 8h).

Visual stimulation

A white organic light-emitting display (OLEDXL, eMagin, Bellevue, WA; 800 X 600 pixel resolution, 60 Hz refresh rate) was controlled by an Intel Core Duo computer with a Windows 7 operating system and was presented to the retina at a resolution of 1.1

μm/pixel. Visual stimuli were generated using MATLAB and the Psychophysics Toolbox, and were projected through the condenser lens of the two-photon microscope focused on the photoreceptor layer.

For the peripheral spot experiments, stationary spots of size 110 μm diameter were presented 165 μm away from the soma of the recorded pDGSC for 2 seconds. At this distance, these spots were presented outside of the dendritic span of the majority of recorded pDSGCs. These spots were presented in 8 different locations pseudorandomized around the recorded pDSGC, with 3 repetitions each.

For moving bar experiments, a bright moving bar with dimensions 110 μm (width) X 880 μm (length) and speed 330 μm/s moved in 8 different pseudorandomized directions across the receptive field of the pDSGC, with 3 – 6 repetitions each. The occluded bar stimulus contains a moving bar of the same dimensions which moves into and out of a central occluder with a diameter size of 220 μm. The size of the occluder was large enough to obscure the entire dendritic span for the majority of recorded pDSGCs. Occluded bar stimuli of different contrasts were used. The population vector model in **Figure 7** required the use of bar and occluded bar stimuli at speeds of 330 μm/s, 660 μm/s, 1320 μm/s, 1980 μm/s, and 2640 μm/s.

For the emergent moving bar experiments where the bar emerged from different locations of the receptive field, a bright moving bar with dimensions 110 μm (width) X 440 μm (length) and speed 330 μm/s could start moving pseudorandomly from 13 different locations across the receptive field (Figure 5). The bar could move in the preferred or null direction of the recorded cell.

For the receptive field mapping experiments measuring spiking activity, bright spots with a 60 μm diameter were presented across the receptive field of the recorded pDSGC. They were shown for 3 – 4 repetitions with a duration of 400 ms in a random sequence within an 11 X 11 grid, covering a total area of 660 X 660 μm^2. For the receptive field mapping experiments measuring EPSC activity, bright spots with a 20 μm diameter were presented across the pDSGC and were shown for 3 – 4 repetitions with a duration of 400 ms in a random sequence within an 11 X 11 grid, covering a total area of 220 X 220 μm^2. To examine the kinetics of EPSCs, bright spots with either a 20 μm diameter (for DHβE and gabazine experiments) or a 60 μm diameter (for DHβE experiments) were shown across the receptive field in a random sequence within an 11 X 11 grid for 3 – 4 repetitions. Spots were shown with a duration of 400 ms.

The light intensity for bright peripheral spot experiments, the moving bar and occlusion experiments, and the receptive field mapping experiments was ~1.6×10^4 R*/rod/s.

735 **Targeting cells for electrophysiology**
736 Cells were visualized with infrared light (>900 nm) and an IR-sensitive video camera
737 (Watec). DSGCs were targeted with the aid of two-photon microscopy in *Drd4-GFP*
738 mice. Cell identity was confirmed physiologically by extracellular recordings of
739 responses to moving bars and/or by filling the cell with 25 μM Alexa 594 (Life
740 Technologies) to show bistratified dendritic morphology. Because the tissue was aligned
741 on the filter paper, we confirmed that the preferred direction of the spiking responses to
742 moving bar aligned well with the anatomical posterior (visual field coordinate) or nasal
743 (retinal coordinate) direction.
744
745 **Quantification of dendritic morphology**
746 The On and Off layers of each cell was isolated from a z-stacked image in ImageJ. To
747 calculate the radius, a contour of the dendritic span was made by drawing a boundary
748 around the dendritic tips, and the area within the contour and resulting equivalent radius
749 was calculated. For calculating dendritic length, the On layer from the z-stack projection
750 was traced in NeuronStudio. The two-dimensional trace was then exported to MATLAB.
751 Dendritic length was calculated in MATLAB using a custom-written code. We subdivided
752 the cell into eight sectors for analysis. Sectors extended out from the soma and were
753 aligned to the spot stimulus such that each spot was at the center between each
754 sector's radial boundaries. When computing normalized vector sums (Figures 2B – C,
755 S2A – S2B), total dendritic length in each sector was normalized by the total dendritic
756 length of the cell.
757
758 **Serial electron-microscopic analysis**
759 We reconstructed DSGCs and starburst amacrine cells from a previously published
760 SBEM dataset (Ding et al., 2016). These cell types were easily recognizable from their
761 characteristic dendritic arbors and patterns of stratification. We inferred the preferred
762 direction of motion of the DSGCs, relative to the boundaries of the volume from the
763 orientation of SAC dendritic inputs onto the DSGC dendrites, as in Briggman et al.
764 (2011). SAC dendrites preferentially form GABAergic synapses with DSGCs if their
765 orientation, from soma to dendritic tip, corresponds to the null direction of the DSGC.
766 Neither the eye of origin nor the retinal location of the sample was recorded when this
767 sample was acquired, but it was possible to infer the ventral direction within the volume
768 from reconstructions of multiple members of several other RGC types with strong
769 dendritic asymmetries along the dorsoventral axis, including Jam-B RGCs (Kay et al.,
770 2011) and F-RGCs (Rousso et al., 2016). One of the four On-Off DSGC types had an
771 inferred preference for the ventral direction. Thus, we infer that the two types with
772 preferred directions 90 degrees away from this ventral-motion-preferring DSGC type
773 must therefore have been tuned to the horizontal motion axis. We could think of no way

774 to distinguish which of these types prefers anterior motion and which prefers posterior
775 motion.
776
777 Ribbon synapses from On bipolar cells onto the dendrites of these three DSGCs were
778 mapped manually. The branching patterns of all cells were reconstructed using
779 skeletons and synapses were marked with single nodes using the Knossos software
780 package (https://knossostool.org/).
781
782 To measure local ribbon density across the DSGC dendritic field, the dendritic span was
783 divided into individual squares with 10 x 10 µm (Figure S4) or 20 x 20 µm (Figure 4)
784 dimensions. Total dendritic length in each square was calculated in Matlab with a
785 custom-written code. The total number of ribbon synapses in each square was also
786 quantified. Ribbon density was calculated by dividing the ribbon synapse number by the
787 total dendritic length in the appropriate squares.
788
789 **Electrophysiology recordings**
790 Recording electrodes of 3 – 5 MΩ were filled with a cesium-based internal solution
791 containing 110 mM CsMeSO4, 2.8 mM NaCl, 4 mM EGTA, 5 mM TEA-Cl, 4 mM
792 adenosine 5′-triphosphate (magnesium salt), 0.3 mM guanosine 5′-triphosphate
793 (trisodium salt), 20 mM HEPES, 10 mM phosphocreatine (disodium salt), 5 mM N-
794 Ethyllidocaine chloride (QX314),filled with a cesium-based internal solution containing
795 110 mM CsMeSO4, 2.8 mM NaCl, 4 mM EGTA, 5 mM TEA-Cl, 4 mM adenosine 5′-
796 triphosphate (magnesium salt), 0.3 mM guanosine 5′-triphosphate (trisodium salt), 20
797 mM HEPES, 10 mM phosphocreatine (disodium salt), 5 mM N-Ethyllidocaine chloride
798 (QX314), and 0.025 mM Alexa 594, pH 7.25. Retinas were kept in oxygenated Ames'
799 medium with a bath temperature of 32 – 34 °C.
800
801 Data were acquired using PCLAMP 10 and a Multiclamp 700B amplifier (Molecular
802 Devices, Sunnyvale, CA), low-pass filtered at 4 kHz and digitized at 10 kHz. Light
803 evoked EPSCs were isolated by holding cells at -60 mV after correction for the liquid
804 junction potential (~10 mV).
805
806 To isolate the contribution of synaptic inputs, a host of pharmacological agents were
807 perfused in the bath during electrophysiology recordings. 8 µM Dihydro-b-erythroidine
808 hydrobromide (DHβE; Tocris, Cat#2349); 10 µM SR 9551 hydrobromide (gabazine;
809 Tocris, Cat #1262); 100 µM Meclofenamic acid sodium salt (MFA; Sigma-Aldrich.
810 Cat#M4531); 1 µM Strychnine (Sigma-Aldrich, Cat#S0532); 50 µM TPMPA (Tocris,
811 Cat#1040; 50 µM Carbenoxolone disodium (Tocris, Cat#3096).
812
813 **Data analysis of electrophysiological recordings**

814 Spiking data from loose-patch recordings were analyzed using custom protocols in
815 MATLAB. The number of spikes evoked by the response to the peripheral spots were
816 quantified in MATLAB and averaged across 3 repetitions in 8 spatial locations. Light-
817 evoked EPSC responses to peripheral spots were obtained as well, and 3 repetitions of
818 EPSC traces were averaged to obtain the mean peak amplitude and charge transfer
819 response to each condition. The RSI is determined by (Max - Opp)/(Max + Opp) where
820 Max is the number of spikes, peak amplitude or charge transfer in the region of maximal
821 activation using the peripheral spot stimulus, and Opp is the response in the region
822 directly opposite to the Max region. EPSC parameters of latency, rise time (10 - 90%),
823 and decay time (90 - 10%) were quantified to compare the whole cell kinetics after
824 administration of DHβE and gabazine to the control condition (Figure S1E).
825
826 For the receptive field mapping experiments, the light-evoked EPSCs in response to
827 spots sized either 20 μm or 60 μm in diameter were obtained and averaged across 3 –
828 4 repetitions. The displacement of the spiking RF was determined by using 60 μm
829 spots. The distance from the soma to the edges of the receptive field on the preferred
830 side versus the null side were determined (Figure S1H).
831
832 For the receptive field mapping EPSC experiments using 20 μm spots, the center of
833 mass of the receptive field was determined using the EPSC charge transfer or
834 amplitude at each square in the 11 X 11 grid. The dendritic length was calculated at
835 each point on the RF stimulus grid by summing the dendritic length in a circle 60 μm in
836 diameter centered on the square of interest. For maximum vs. opposite region analysis
837 and the preferred side vs null side analysis (Figures 3E and 3F), we considered the
838 EPSCs in two 5 X 5 subsets of the total grid located opposite of each other. The
839 preferred-null side of each cell was determined by spiking responses to the full-field
840 moving bar, and the maximum-opposite axis was determined by EPSC charge transfer
841 responses to the peripheral spot experiment performed in DHβE and gabazine. The
842 distance from soma at each grid location was defined as the distance between the
843 center of the square and the soma center.
844
845 To estimate the spatiotemporal profile across the maximum-opposite or the preferred-
846 null axis for cells in DHβE and gabazine, the light-evoked EPSCs in response to small
847 spots sized 20 μm in diameter were obtained and averaged across 3 – 4 repetitions
848 (Figures 4F – 4H). To estimate the spatiotemporal profile across the preferred-null axis
849 for cells in DHβE only, the light-evoked EPSCs in response to small spots sized 60 μm
850 in diameter were obtained and averaged across 3 repetitions (Figures S4C –D). For
851 both experiments, EPSC parameters of latency, rise time (10 - 90%), and decay time
852 (90 - 30%) were quantified. The preferred-null axis of each cell was determined by
853 spiking responses to the full-field moving bar, and the maximum-opposite axis was

854 determined by EPSC charge transfer responses to the peripheral spot experiment
855 performed in DHβE and gabazine. The parameters of latency, rise time, and decay time
856 were averaged across the squares at equal distances along the cell's preferred-null axis
857 or maximum-opposite axis.
858
859 Spiking data evoked by the moving bar and occlusion stimuli were quantified in
860 MATLAB using 3 – 6 repetitions in 8 different directions. Spiking data evoked by the bar
861 starting in different positions were quantified in MATLAB across 3 repetitions in the
862 preferred and null directions.
863
864
865 **Calcium imaging in posterior- and anterior-preferring On-Off DSGCs**
866 Genetically encoded calcium indicator GCaMP6f was expressed in all RGCs by
867 crossing *Vglut2-IRES-Cre* mice (JAX 016963-*Slc17a6*$^{tm2(cre)Lowl}$) and floxed *Ai95(RCL-*
868 *GCaMP6f)-D* mice (JAX 028865-*Gt(ROSA)26Sor*$^{tm95.1(CAG-GCaMP6f)Hze}$/J). GCaMP6f
869 fluorescence from isolated retinas was imaged in a customized two-photon laser
870 scanning fluorescence microscope (Bruker Nano Surfaces Division). GCaMP6 was
871 excited by a Ti:sapphire laser (Coherent, Chameleon Ultra II, Santa Clara, CA) tuned to
872 920 nm, and the laser power was adjusted to avoid saturation of the fluorescent signal.
873 Onset of laser scanning induces a transient response in RGCs that adapts to the
874 baseline in ~3 s. Therefore, to ensure the complete adaptation of this laser-induced
875 response and a stable baseline, visual stimuli were given after 10 s of continuous laser
876 scanning. To separate the visual stimulus from GCaMP6 fluorescence, a band-pass
877 filter (Semrock, Rochester, MA) was placed on the OLED to pass blue light peaked at
878 470 nm, while two notched filters (Bruker Nano Surfaces Division) were placed before
879 the photomultiplier tubes to block light of the same wavelength. The objective was a
880 water immersion objective (60x, Olympus LUMPlanFl/IR). Time series of fluorescence
881 were collected at 15–30 Hz.

882 We performed an initial direction selectivity test to identify posterior- and anterior-
883 preferring On-Off DSGCs. We recorded GCaMP6f fluorescence from RGC somas within
884 a 75-μm X 75-μm field of view while presenting a full-field moving bar visual stimulus (a
885 bright moving bar 110 μm (width) X 880 μm (length) moving at 330 μm/s across a 660
886 μm circular mask diameter along 8 different directions). At the onset of each moving bar
887 sweep, a TTL pulse was triggered by the visual stimulus computer and recorded by the
888 imaging software to correlate GCaMP6f signals with the direction of each moving bar.
889 Immediately following acquisition of each time series stack, custom-written MATLAB
890 scripts were used to extract fluorescence over time data from time-series images and
891 sort calcium transient by direction of the moving bar. For each RGC soma, raw
892 GCaMP6f fluorescence traces and tuning curves were plotted. On-Off DSGCs were
893 identified by their characteristic singular-lobe directional tuning curves, DSI values ≥ 0.3,

894 and two fluorescence peaks time-locked to the leading (On) and trailing edge (Off) of
895 the moving bar. On-Off DSGCs with preferred directions along the posterior-anterior
896 axis were then selected for further imaging.

897 Once an On-Off DSGC of interest was identified, the visual stimulus was centered to the
898 soma of that cell and a new field of view was drawn to enclose this cell and some
899 background with no GCaMP6f fluorescence. Full-field and occlusion moving bar visual
900 stimulus were presented to the cells as described above (8 directions, 3-4 repetitions).
901 Time series data was collected and subjected to offline analysis.

902 **Imaging analysis for calcium imaging**
903 Analysis was performed using ImageJ and MATLAB. Regions of interest (ROIs)
904 corresponding to DSGC soma and background were manually selected in ImageJ. The
905 fluorescent time course of each ROI was determined by averaging all pixels within the
906 ROI for each frame. The fluorescence of the background region was subtracted from
907 the raw fluorescent signal of the soma ROIs at each time frame. The visual stimulus
908 included a 3 – 4 second intersweep interval between the end of one sweep and the start
909 of another. Fluorescence intensities during these intersweep intervals were used to
910 create a baseline (F0) trace for each ROI by fitting either a single- or two-term
911 exponential decay function. Fluorescence measurements were then converted to $\Delta F/F0$
912 values by calculating $\Delta F=(F-F0)/F0$ for every datapoint. The transformed traces were
913 then smoothed using an average sliding window of 4 datapoints. $\Delta F/F0$ traces were
914 clipped, sorted by visual stimulus direction (0, 45, 90, 135, 180, 225, 270, and 315
915 degrees), and averaged over 3-4 trials. Prior to further analysis, ROIs were subjected
916 to a response quality test $QI = Var[Avg.\ Resp]/Avg(Var[R(t)]) \geq 0.45$ to ensure
917 consistency across trials. Responses to the full-field and occlusion moving bars were
918 broken up into On and Off components according to the circular mask entrance and exit
919 times of the leading and trailing edge, respectively. Peak, area $\Delta F/F0$, and time of peak
920 values were calculated for On, Off, and the full trace along all 8 directions. Direction
921 selectivity index (DSI), vector sum, and preferred direction were calculated for both On
922 and Off components.
923
924 **Statistical analysis**
925 Grouped data are presented as mean ± SEM. The Kolmogorov-Smirnov test was used
926 to test data for normality. Student's t-test was used for statistical comparisons of paired
927 samples in Figures 1 and 2. One-way analysis of variance was performed on grouped
928 data in Figures 5 and 6 and subjected to Bonferroni correction.
929
930 For the EPSC/dendritic length vs distance from soma experiments, we performed linear
931 regression analysis using an additional categorical predictor variable indicating the
932 maximum-opposite or the preferred-null side. The p-value associated with interaction

term (distance*region) in the resulting model was used to determine whether the slopes are significantly different between the two regions. For the EPSC vs dendritic length experiments, we again performed linear regression with an additional categorical predictor variable indicating the maximum-opposite or preferred-null region. The p-value associated with the categorical predictor in the resulting model was used to determine whether the y-intercepts were significantly different between the two regions. The p-value associated with the categorical predictor was used to determine whether the y-intercepts were significantly different between regions. The number of branches in each square of the grid was determined by a custom MATLAB code.

For the kinetic analyses of EPSC parameters in the receptive field mapping experiments of latency, rise time, and decay time, we performed linear regression analysis to determine whether a statistically significant linear relationship exists between the distance from the soma and each EPSC parameter.

For all data sets, $p < 0.05$ was considered significant. *$p < 0.05$; **$p < 0.01$; ***$p < 0.001$.

Experimental parameters for population model

Experimental data for the spiking response to full-field (73 cells) and occlusion (69 cells) stimuli moving with a constant speed of 330 μm/second were obtained. 3 – 6 repetitions were obtained for each full-field or occlusion protocol. The baseline firing rate for each repetition was obtained by binning the spiking response in 25-ms time bins and taking the maximum firing rate during a silent period where no stimulus was displayed, and the baseline firing rate was averaged across all repetitions.

To model the spiking response of the pDSGCs, we binned the spikes evoked by the On response to the motion stimulus in 25-ms time bins and plotted the PSTHs for all 8 motion directions. Then, we fit a rectified sine wave to the PSTH of each pDSGC. We defined the threshold for above-baseline firing to be 4 SD above the baseline firing rate. The onset of the spiking response was determined by the time bin at which the firing rate exceeded the threshold and was immediately followed by a second above-threshold bin (Rate change method; Levakova et al., 2015). We inspected the spiking response onset times returned by our detection algorithm and manually adjusted the spiking response onset times for 3 out of 91 pDSGCs to match the experimental data.

Onset times of spiking responses to the full-field bar moving in the preferred direction ± 45 degrees were similar to those of the preferred-direction response (Figure S7A, left). Likewise, onset times of spiking responses to the occlusion stimulus moving in the null direction ± 45 degrees were similar to those of the null-direction response (Figure S7A, right). Therefore, we included onset times of spiking responses to motions in the

973 directions ± 45 degrees from the preferred-null motion axis in our analysis. Four-
974 parameter beta distributions were fit to histograms of spiking response onset times for
975 preferred- and null-direction motions (Figure S7F). The four parameters included two
976 shape parameters and two parameters that specify the minimum and maximum of the
977 distribution's range.
978
979 To determine the offset of the spiking response, we used the algorithm for identifying
980 spiking response onset. Unlike the protocol for determining spiking response onset,
981 however, the detection algorithm started from the most recent time bin and traversed
982 backwards in time. The offset of the spiking response was defined to be the time bin at
983 which the firing rate exceeded the threshold in two out of three consecutive time bins.
984 For each pDSGC, we calculated the spiking response duration by finding the difference
985 between the spiking response onset and offset times. Furthermore, we calculated the
986 linear correlation between spiking response duration and onset (Figure S7G). Figure
987 S7B shows that using only spiking responses to motion along the preferred-null motion
988 axis and using spiking responses to motion along the preferred-null motion axis as well
989 as motion in the directions 45 degrees away from the preferred-null motion axis yielded
990 consistent results. We also calculated the linear correlation between peak firing rate and
991 spiking response onset, but the correlation was not significant for the full-field protocol
992 (Figure S7C).
993
994 **Motion direction tuning curves**
995 We computed motion direction tuning curves for all pDSGCs exposed to the full-field
996 moving bar stimulus (73 cells) using the CircStat toolbox in MATLAB developed by P.
997 Berens (2009). The height of each tuning curve was given by the total spike count
998 evoked during the presentation of the full-field moving bar stimulus. We fit a Gaussian
999 function to the histogram of the tuning curve widths (Figure S7H). Figure S7I shows all
1000 the normalized motion direction tuning curves. The heights of the tuning curves were
1001 rescaled by dividing by their peaks and the widths of the tuning curves were rescaled by
1002 dividing by their angular deviation, which is the square-root of twice the circular
1003 variance. The normalized tuning curves were fit to a one-term Gaussian model (Figure
1004 S7I).
1005
1006 **Speed Tuning Analysis**
1007 To investigate whether the null-direction response remains robust at higher stimulus
1008 speeds, experimental data for the spiking response to full-field and occlusion stimuli
1009 moving at 660, 1320, 1980, and 2640 μm/s were further collected. We analyzed how the
1010 spike count, onset, and duration of the null-direction response changed across bar
1011 speeds (Figure S7J–L). Spiking response onset and offset were calculated using the
1012 same method as before. Linear fits were performed on spiking response onset data

across speeds for both full-field and occlusion protocols (Figure S7K). Spiking response durations were first normalized by the response duration when the bar speed was at 330 μm/s and then fit to power-law functions (Figure S7L). Simulation parameters for stimulus speeds higher than 330 μm/s were adjusted according to the fit functions in Figure S7K and L.

Two-dimensional population model

In our computational model, we arranged two populations (left motion-preferring and right motion-preferring) of DSGCs in a two-dimensional array. Each population had 1,000 cells. Within each population, horizontal and vertical distances between nearest neighbors were Gaussian distributed, with a mean of 39 μm and a SD of 16 μm (Huberman et al., 2009). The spatial positions of the DSGCs between the two populations were uncorrelated.

Each DSGC's mean spiking response to the moving edge was modeled as a rectified sine wave. The amplitude of the sine wave was given by the peak firing rate, while the period and phase were determined by the spiking response duration and onset time, respectively. For each spatial arrangement of DSGCs, we sampled peak firing rates directly from our experimental data. We sampled spiking response onset times from our four-parameter beta distributions (Figure S7F) and determined the spiking response durations by finding the linear correlation between the two (Figure S7G). For simulations with bar stimuli moving at speeds higher than 330 μm/s, spiking response onset times and durations were modified according to the speed of the bar (Figure S7K and L).

Noise was introduced into the preferred directions of the DSGCs so that they were not all perfectly aligned with the left/right motion axis. To determine the degree of jitter in a DSGC's preferred direction, we sampled from a uniform distribution ranging from -14.1 degrees to +14.1 degrees, where 0 degrees represented a preference for motion directly along the left/right motion axis (Fiscella et al., 2015).

To determine the motion direction tuning width of each simulated DSGC, we sampled circular variances from a Gaussian distribution fit to the histogram of circular variance of the tuning curves from our experimental data (Figure S7H). We scaled the collapsed tuning curve (Figure S7I) by the sampled tuning width and peak firing rate to obtain the tuning curve. We used the motion direction tuning curve to adjust the peak firing rate of the spiking response according to the jitter in the preferred direction alignment.

We simulated the DSGC population response to a moving edge traveling from left to right at a constant speed. To simulate the occlusion protocol, we introduced an occlusion 220 μm in diameter whose position in space was fixed at 1800 μm along the

horizontal axis and 800 μm along the vertical axis (approximately in the center of the two-dimensional array). For each spatial arrangement of DSGCs, the simulation was repeated 10 times. The spiking response of each DSGC was discretized in time.

At each 10-ms time bin, the firing rate given by the rectified sine wave fit was converted to a mean spike count. The number of spikes generated by a DSGC was obtained by sampling from a Gaussian distribution with this mean and a sub-Poisson, constant variance of 0.4. The sub-Poisson noise was determined from our experimental data by analyzing the variance of the spiking responses to 6 repetitions of the full-field moving bar (10 cells) and the occlusion stimulus (9 cells) (Figure S7D). The spatial positions of the DSGCs were shuffled in each simulation block for a total of 100 blocks with 10 repetitions in each block.

Position decoding

The spatial position of the moving bar's leading edge was estimated via a labeled-line decoder (Dayan and Abbott, 2001). At each time point, the position estimate $\hat{x}$ was given by the weighted average of the DSGCs' RF center positions

$$\hat{x} = \frac{\sum_i r_i \tilde{x}_i / w_i^2}{\sum_i r_i / w_i^2}$$

where r_i is the firing rate of the ith cell and $\tilde{x}_i \sim \mathcal{N}(x_i, {w_i}^2)$ where x_i is the RF center position and w_i the RF width (radius) of the ith cell. The RF width was taken to be the 1 SD boundary of the Gaussian center profile (Chichilnisky and Kalmar, 2002). RF widths were obtained by scaling the dendritic field radii by 1.25. Dendritic field radii were obtained by sampling from Gaussian distribution with $\mu = 88$ μm and $\sigma = 14.8$ μm. Position labels of the cells were determined by considering the extent of spatial displacement on the preferred side. Errors are reported as the root mean-square-error in the position estimate (Figure 7B).

Coincidence detection

To assess the salience of the synchronous firing between two oppositely tuned subtypes of DSGCs, we constructed a coincidence decoder that consisted of a convolution with a temporal filter and a threshold operation, similar to Schwartz et al., 2007. At each time point, a difference-of-Gaussian temporal filter (Figure 7E) was convolved with the simulated DSGC population firing-rate activity. When the output of the convolution exceeded the threshold, the decoder determined that a coincidence of spiking activity between DSGC subtypes has occurred. For correct detections, the output must exceed the threshold during a time window of 125 ms around the occlusion

event when the bar emerges from behind the occluder (Figure 7F). All above-threshold outputs outside of the time window were marked as false alarms. By varying the threshold across multiple simulations, we computed the receiver operator characteristic (ROC) (Green and Swets, 1966). We quantified the performance of the decoder under different levels of background firing noise using the area under the ROC curve (Figure 7G).

References

Barlow, H. B. and Hill, R. M. (1963). Selective sensitivity to direction of movement in ganglion cells of rabbit retina. *Science* **139**, 412–414.

Barlow, H.B., and Levick, W.R. (1965). The mechanism of directionally selective units in rabbit's retina. *J. Physiol*. **178**, 477–504.

Basso, M.A., Bickford, M.E., and Cang, J. Unraveling circuits of visual perception and cognition through the superior colliculus. *Neuron* **109**, https://doi.org/10.1016/j.neuron.2021.01.013

Briggman, K.L., Helmstaedter, M., and Denk, W. (2011). Wiring specificity in the direction-selectivity circuit of the retina. *Nature* **471**, 183–188.

Chen, Q., Pei, Z., Koren, D., and Wei, W. (2016). Stimulus-dependent recruitment of lateral inhibition underlies retinal direction selectivity. *Elife* **5**, e21053.

Chen, Q., Smith, R.G., Huang, X., and Wei, W. (2020). Preserving inhibition with a disinhibitory microcircuit in the retina. *Elife* **9**, e62618.

Chiao, C.C., and Masland, R.H. (2003). Contextual tuning of direction-selective retinal ganglion cells. *Nat. Neurosci*. **6**, 1251–1252.

Chichilnisky, E.J. and Kalmar, R.S. (2002). Functional asymmetries in ON and OFF ganglion cells of primate retina. *J. Neurosci.* **22**, 2737–2747.

Cruz-Martín, A., El-Danaf, R.N., Osakada, F., Sriram, B., Dhande, O.S., Nguyen, P.L., Callaway, E.M., Ghosh, A., and Huberman, A.D. (2014). A dedicated circuit links direction-selective retinal ganglion cells to the primary visual cortex. *Nature* **507**, 358–361.

Dayan, P. and Abbott, L. (2001). Theoretical neuroscience - computational and mathematical modeling of neural systems. Cambridge, MA: MIT Press.

Demb, J. B., Haarsma, L., Freed, M. A. and Sterling, P. (1999). Functional circuitry of the retinal ganglion cell's nonlinear receptive field. *J. Neurosci.* **19**, 9756–9767.

Deny, S., Ferrari, U., Macé, E., Yger, P., Caplette, R., Picaud, S., Tkačik, G., and Marre, O. (2017). Multiplexed computations in retinal ganglion cells of a single type. *Nat. Commun.* **8**, 1964.

Dhande, O.S., Stafford, B.K., Lim, J.-H.A., and Huberman, A.D. (2015). Contributions of retinal ganglion cells to subcortical visual processing and behaviors. *Annu. Rev. Vis. Sci.* **1**, 291–328.

Ding, H., Smith, R.G., Poleg-Polsky, A., Diamond, J.S., and Briggman, K.L. (2016). Species-specific wiring for direction selectivity in the mammalian retina. *Nature* **535**, 105–110.

Ellis, E.M., Gauvain, G., Sivyer, B., and Murphy, G.J. (2016). Shared and distinct retinal input to the mouse superior colliculus and dorsal lateral geniculate nucleus. *J. Neurophysiol.* **116***,* 602–610.

El-Quessney, M., Maanum, K., and Feller, M.B. (2020). Visual experience influences dendritic orientation but is not required for asymmetric wiring of the retinal direction selective circuit. *Cell Rep.* **31**, 107844.

Euler, T., Detwiler, P. B. and Denk, W. (2002). Directionally selective calcium signals in dendrites of starburst amacrine cells. *Nature* **418**, 845–852.

Famiglietti, E. V. (1983). "Starburst" amacrine cells and cholinergic neurons: mirror-symmetric ON and OFF amacrine cells of rabbit retina. *Brain Res.* **261**, 138–144.

Fiscella, M., Franke, F., Farrow, K., Müller, J., Roska, B., da Silveira, R.A., and Hierlemann, A. (2015). Visual coding with a population of direction-selective neurons. *J. Neurophysiol.* **114**, 2485–2499.

Franke, K., Berens, P., Schubert, T., Bethge, M., Euler, T., and Baden, T. (2017). Inhibition decorrelates visual feature representations in the inner retina. *Nature* **542**, 439–444.

Fried, S.I., Münch, T.A., and Werblin, F.S. (2002). Mechanisms and circuitry underlying directional selectivity in the retina. *Nature* **420**, 411–414.

Green, D. M., and Swets, J. A. (1966). *Signal detection theory and psychophysics.* John Wiley.

Grzywacz, N.M., and Amthor, F.R. (2007). Robust directional computation in on-off directionally selective ganglion cells of rabbit retina. *Vis. Neurosci.* **24**, 647–661.

He, S., Jin, Z.F., and Masland, R.H. (1999). The nondiscriminating zone of directionally selective retinal ganglion cells: comparison with dendritic structure and implications for mechanism. *J. Neurosci.* **19**, 8049–8056.

He, S., and Masland, R.H. (1998). ON direction-selective ganglion cells in the rabbit retina: Dendritic morphology and pattern of fasciculation. *Vis. Neurosci.* **15**, 369–375.

Huang, X., Rangel, M., Briggman, K.L., and Wei, W. (2019). Neural mechanisms of contextual modulation in the retinal direction selective circuit. *Nat. Commun.* **10**, 2431.

Huberman, A.D., Wei, W., Elstrott, J., Stafford, B.K., Feller, M.B., and Barres, B.A. (2009). Genetic identification of an On-Off direction- selective retinal ganglion cell subtype reveals a layer-specific subcortical map of posterior motion. *Neuron* **62**, 327–334.

Ishikane, H., Gangi, M., Honda, S., Tachibana, M. (2005). Synchronized retinal oscillations encode essential information for escape behavior in frogs. *Nat. Neurosci.* **8**, 1087–1095.

Ito, S., and Feldheim, D.A. (2018). The mouse superior colliculus: An emerging model for studying circuit formation and function. *Front. Neural Circuits* **12**, 10.

Jacoby, J. and Schwartz, G.W. (2017). Three small-receptive-field ganglion cells in the mouse retina are distinctly tuned to size, speed, and object motion. *J Neurosci.* **37**, 610–625.

Kay, J.N., de la Huerta, I., Kim, I.J., Zhang, Y., Yamagata, M., Chu, M.W., Meister, M., and Sanes, J.R. (2011). Retinal ganglion cells with distinct directional preferences differ in molecular identity, structure, and central projections. *J. Neurosci.* **31**, 7753–7762.

1209 Kim., I.J., Zhang, Y., Meister, M., and Sanes, J.R. (2010). Laminar restriction of retinal
1210 ganglion cell dendrites and axons: subtype-specific development patterns revealed with
1211 transgenic markers. *J. Neurosci* **30**, 1452–1462.
1212
1213 Kim, T., Soto, F., and Kerschensteiner, D. (2015). An excitatory amacrine cell detects
1214 object motion and provides feature-selective input to ganglion cells in the mouse retina.
1215 *Elife* **4**, e08025.
1216
1217 Kittila, C.A., and Massey, S.C. (1997). Pharmacology of directionally selective ganglion
1218 cells in the rabbit retina. *J. Neurophysiol.* **77**, 675–689.
1219
1220 Kühn, N.K., and Gollisch, T. (2019). Activity correlations between direction-selective
1221 retinal ganglion cells synergistically enhance motion decoding from complex visual
1222 scenes. *Neuron* **101**, 963–976.
1223
1224 Lee, S., Kim, K., and Zhou, Z.J. (2010). Role of ACh-GABA cotransmission in detecting
1225 image motion and motion direction. *Neuron* **51**, 787–799.
1226
1227 Lee, S., Zhang, Y., Chen, M., and Zhou, Z.J. (2016). Segregated glycine-glutamate co-
1228 transmission from vGluT3 amacrine cells to contrast-suppressed and contrast-
1229 enhanced retinal circuits. *Neuron* **90**, 27–34.
1230
1231 Levakova, M., Tamborrino, M., Ditlevsen, S., and Lansky, P. (2015). A review of the
1232 methods for neuronal response latency estimation. *Biosystems* **136**, 23–34.
1233
1234 Lipin, M.Y., Rowl Taylor, W., and Smith, R.G. (2015). Inhibitory input to the direction-
1235 selective ganglion cell is saturated at low contrast. *J. Neurophysiol.* **114**, 927–941.
1236
1237 Marre, O., Botella-Soler, V., Simmons, K.D., Mora, T., Tkačik, G., and Berry, M.J.
1238 (2015). High accuracy decoding of dynamical motion from a large retinal population.
1239 *PLoS Comput. Biol.* **11**, e1004304.
1240
1241 Matsumoto, A., Briggman, K.L., and Yonehara, K. (2019). Spatiotemporally asymmetric
1242 excitation supports mammalian retinal motion sensitivity. *Curr. Biol.* **29**, 3277–3288.
1243
1244 Ölveczky, B. P., Baccus, S. A. and Meister, M. (2003). Segregation of object and
1245 background motion in the retina. *Nature* **423**, 401–408.
1246
1247 Oyster, C.W., (1968). The analysis of image-motion by the rabbit retina. *J Physiol.* **199**,
1248 613-635.

1249 Oyster, C.W., and Barlow, H.B. (1967). Direction-selective units in rabbit retina:
1250 Distribution of preferred directions. *Science* **155**, 841–842.
1251
1252 Rivlin-Etzion M., Zhou K., Wei W., Elstrott J., Nguyen P.L., Barres B.A., Huberman A.D.,
1253 and Feller M.B. (2011). Transgenic mice reveal unexpected diversity of On-Off
1254 direction-selective retinal ganglion cell subtypes and brain structures involved in motion
1255 processing. *J Neurosci.* **31**, 8760–8769.
1256
1257 Rousso, D.L.L., Qiao, M., Kagan, R.D.D., Yamagata, M., Palmiter, R.D.D., and Sanes,
1258 J.R.R. (2016). Two pairs of ON and OFF retinal ganglion cells are defined by
1259 intersectional patterns of transcription factor expression. *Cell Rep*. **15**, 1930–1944.
1260
1261 Sabbah, S., Gemmer, J.A., Bhatia-Lin, A., Manoff, G., Castro, G., Siegel, J.K., Jeffery,
1262 N., and Berson, D.M. (2017). A retinal code for motion along the gravitational and body
1263 axes. *Nature* **546**, 492–497.
1264
1265 Sanes, J.R. and Masland R.H. (2015). The types of retinal ganglion cells: current
1266 Status and implications for neuronal classification. *Ann. Rev. Neurosci.* **38**, 221–246.
1267
1268 Schwartz, G., Taylor, S., Fisher, C., Harris, R., and Berry, M.J., II (2007). Synchronized
1269 firing among retinal ganglion cells signals motion reversal. *Neuron* **55**, 958–969.
1270
1271 Sethuramanujam, S., McLaughlin, A.J., deRosenroll, G., Hoggarth, A., Schwab, D.J.,
1272 and Awatramani, G.B. (2016). A central role for mixed acetylcholine/GABA transmission
1273 in direction coding in the retina. *Neuron* **90**, 1243–1256.
1274
1275 Simpson, JI., Leonard, C.S., and Soodak, R.E. (1984). The accessory optic system.
1276 *Ann. Rev. Neurosci*. **7**, 13-41.
1277
1278 Sivyer, B., van Wyk, M., Vaney, D.I., and Taylor, W.R. (2010). Synaptic inputs and
1279 timing underlying the velocity tuning of direction-selective ganglion cells in rabbit retina.
1280 *J. Physiol.* **588**, 3243–3253.
1281
1282 Shang, C., Liu, L., Chen, Z., Shi, Y., Wang, Q., Liu, S., Li, D., and Cao, P. (2015). A
1283 parvalbumin-positive excitatory visual pathway to trigger fear responses in mice.
1284 Science **348**, 1472–1477.
1285
1286 Shi, X., Barchini, J., Ledesma, H.A., Koren, D., Jin, Y., Liu, X., Wei, W., and Cang, J.
1287 (2017). Retinal origin of direction selectivity in the superior colliculus. *Nat. Neurosci.* **20**,
1288 550–558.

Spruston, N. (2008). Pyramidal neurons: dendritic structure and synaptic integration. *Nat. Neurosci. Reviews* **9**, 206–221.

Takeshita, D., and Gollisch, T. (2014). Nonlinear spatial integration in the receptive field surround of retinal ganglion cells. *J. Neurosci.* **34**, 7548–7561.

Taylor, W.R., and Vaney, D.I. (2002). Diverse synaptic mechanisms generate direction selectivity in the rabbit retina. *J. Neurosci.* **22**, 7712–7720.

Trenholm, S., Johnson, K., Li, X., Smith, R.G., and Awatramani, G.B. (2011). Parallel mechanisms encode direction in the retina. *Neuron* **71**, 683–694.

Turner, M.H., Schwartz, G.W., and Rieke, F. (2018). Receptive field center-surround interactions mediate context-dependent spatial contrast encoding in the retina. *Elife* **7**, e38841.

Wei, W., Hamby, A.M., Zhou, K., and Feller, M.B. (2011). Development of asymmetric inhibition underlying direction selectivity in the retina. *Nature* **469**, 402–406.

Wyatt, H.J., and Daw, N.W. (1975). Directionally sensitive ganglion cells in the rabbit retina: specificity for stimulus direction, size and speed. *J. Neurophysiol.* **38**, 613–626.

Yonehara, K., Balint, K., Noda, M., Nagel, G., Bamberg, E., and Roska, B. (2011). Spatially asymmetric reorganization of inhibition establishes a motion-sensitive circuit. *Nature* **469**, 407–410.

Zhang, Y., Kim, I.J., Sanes, J.R., and Meister, M. (2012). The most numerous ganglion cell type of the mouse retina is a selective feature detector. *Proc. Natl. Acad. Sci. U. S. A.* **109**, E2391–E21398.

Zylberberg, J., Cafaro, J., Turner, M.H., Shea-Brown, E., and Rieke, F. (2016). Direction-selective circuits shape noise to ensure a precise population code. *Neuron* **89**, 369–383.